RESEARCH ARTICLE | MAY 02 2024

Role of spontaneous thermal emissions in inflationary laser Raman instability

B. Eliasson ; M. E. Dieckmann ; X. Y. Jiang ; Z. M. Sheng ; C. S. Liu

Phys. Plasmas 31, 053303 (2024)
https://doi.org/10.1063/5.0188949

Role of spontaneous thermal emissions in inflationary laser Raman instability

Cite as: Phys. Plasmas **31**, 053303 (2024); doi: 10.1063/5.0188949
Submitted: 25 November 2023 · Accepted: 20 April 2024 ·
Published Online: 2 May 2024

B. Eliasson,[1,a)] M. E. Dieckmann,[2] X. Y. Jiang,[3,4] Z. M. Sheng,[3,4,5] and C. S. Liu[6]

AFFILIATIONS

[1]University of Strathclyde, SUPA, Glasgow G4 0NG, Scotland, United Kingdom
[2]Department of Science and Technology (ITN), Linköping University, Campus Norrköping, SE-60174 Norrköping, Sweden
[3]Key Laboratory for Laser Plasmas (MOE), School of Physics and Astronomy, Shanghai Jiao Tong University, Shanghai 200240, China
[4]Collaborative Innovation Center of IFSA (CICIFSA), Shanghai Jiao Tong University, Shanghai 200240, China
[5]Tsung-Dao Lee Institute, Shanghai Jiao Tong University, Shanghai 200240, China
[6]University of Maryland, College Park, Maryland 20742, USA

[a)]**Author to whom correspondence should be addressed:** bengt.eliasson@strath.ac.uk

ABSTRACT

The role of thermal fluctuations on the stimulated Raman backscattering instability is investigated by means of Vlasov and particle-in-cell (PIC) simulations in a regime of strong linear Landau damping of the Langmuir wave. The instability is initially convective and amplifies thermal noise, leading to a low-amplitude back-scattered laser sideband. Linear Landau damping of the Langmuir sideband modifies and flattens the electron velocity distribution function at the resonant velocity, leading to a gradual decrease in the Landau damping rate and an increase in the convective amplification. The Langmuir wave traps electrons resulting in a rapid nonlinear absolute instability and large amplitude flashes of backscattered light off large amplitude Langmuir waves with trapped electrons, leading to the production of hot electrons. Conditions for simulating realistic thermal noise with Vlasov and PIC simulations are discussed and defined.

I. INTRODUCTION

Understanding and controlling parametric instabilities are of utmost importance for inertial confinement fusion (ICF) experiments,[1,2] laser-based charged particle accelerators,[3] and laser amplification schemes.[4–6] Examples of parametric instabilities relevant for ICF are the stimulated Brillouin scattering (SBS) instability, stimulated Raman backscattering (SRBS) instability,[7,8] and other types of instabilities.[2,9–11] While SBS and filamentation can cause cross beam energy transfer between different laser beams,[12–14] SRBS can lead to energy loss of the incident laser and to unwanted production of hot electrons.[15–17] Rosenberg *et al.*[18] reported results at the National Ignition Facility (NIF) on stimulated Raman scattering (SRS) from direct-drive ignition scale plasma. Strong signals were observed around twice the injected wavelength (i.e., half the injected frequency), indicating absolute SRS at quarter critical density.[19] The mitigation of parametric instabilities by means of broadband lasers[20,21] and the generation of broadband electromagnetic (EM) emissions[22] are active areas of research.

Several encouraging developments have recently been achieved at the NIF facility[23–26] with ignition of compressed pellets of deuterium and tritium. Building on these successes, the efficiency has to be significantly increased for laser fusion to become a viable energy source, and there is a need for enhanced understanding of parametric wave mixing of the laser beams. Several interesting experimental observations of parametric instabilities were made with the Trident Laser Facility[27] in the laser hotspot of a preformed plasma. In particular, "inflation" with a rapid increase in reflectivity of several orders of magnitude to $\sim$1% level when a threshold laser intensity of about $1.5-2.5\times10^{15}$ W/cm^2 was exceeded, and with a saturation of the reflectivity at 5% − 10% for higher laser intensities. These results could not be reproduced using an existing theoretical model for steady-state SRBS in the strong damping regime. In the nonlinear stage of the interaction, a Langmuir decay instability cascade may take place when the large amplitude Langmuir waves from the SRBS instability interact with ion-acoustic waves. The inflation phenomenon was first reported by Fernandez *et al.*[28] and interpreted via particle-in-cell (PIC) simulations by Vu *et al.*,[29,30] who developed a theory for the convective instability when electron trapping is balanced by the velocity space diffusion due to collisions.[31] They suggested that electron trapping in the potential of

the driven plasma wave is the origin of inflation. The time-resolved reflectivity in their PIC simulations showed transient behavior with short spikes of high-amplitude reflected light. On the other hand, the experimental results of Fontaine *et al.*[32] and Michel *et al.*[33] demonstrated that the sharp short wavelength Landau cutoff observed in the backscattered Raman spectra was directly correlated with the instability growing in the absolute regime, but no trapping effects were reported in these experiments. The Landau cutoff was also discussed by Depierreux *et al.*,[34] who reported an experiment with an incident laser and a backscattered seed beam from a reflecting foil. The experiment showed increased Raman amplification of the seed in the regime of initially strong Landau damping, when electron trapping resulted in a significant reduction of the Landau damping.

Wang *et al.*[35] presented a theoretical study of the inflation effect, supported by noiseless grid-based Vlasov simulations. They found that if a low-amplitude resonant laser with a power 10^{-6} of the power of the pump pulse was injected in the opposite direction to seed the SRBS instability, they could reproduce the experimental observations of inflation by Montgomery *et al.*[27] Furthermore, Spencer *et al.*[36] found in PIC simulations that inflationary growth of SRBS far exceeded that of fluid theory for typical parameters in inertial confinement fusion plasmas.

While Wang *et al.*[35] did not address the origin and physics of the resonant seed pulse in their simulations, the results are an important step to understand the physics of the inflation phenomenon. We here suggest that a resonant "seed pulse" could occur naturally due to scattering of the laser off thermal fluctuations in the plasma, enhancing the thermal fluctuations resonantly near the Langmuir wave branch. Three stages of instability can be identified: (1) The resonantly driven Langmuir waves from noise level are initially small amplitude and linearly Landau damped, leading to a slow modification and flattening of the electron distribution function at velocities close to the phase velocity of the resonant Langmuir wave. The result is a gradual decrease in the Landau damping with time and an increase in the convective amplification. (2) As the amplitude of the Langmuir wave increases, it starts trapping electrons in the wave potential,[31] and (3) the instability switches from convective to absolute as described by Wang *et al.*[35] The result is intense transient flashes of reflected light leading to rapid production of hot electrons.

Thermal fluctuations (or noise) occur due to the graininess of the plasma where each particle carries a shielding cloud of opposite charges and gives rise to fluctuations in the electromagnetic fields, which are heavily damped except near eigenmodes of the plasma—the level of the fluctuating electromagnetic field is due to a balance between emission and collective absorption by the plasma particles non-magnetized[37–42] and magnetized[43,44] plasma as a consequence of the fluctuation–dissipation theorem—it is predicted that thermal noise may give rise to enhanced cross-field energy transport in magnetized plasma.[45]

PIC simulations resolve the velocity distribution function statistically with macro-particles,[46] which leads to numerical noise. The numerical noise qualitatively resembles thermal noise,[47,48] but is usually at a much higher amplitude than the real thermal noise in a plasma, since each computational particle represents an ensemble of real particles, increasing the graininess in the simulations compared to that in real plasma. Too high numerical noise levels may cause an unphysically large seed to scatter the laser light and can influence the growth of instabilities. However, by increasing the number of macro-particles, the numerical noise may be reduced to the same level as thermal noise.

On the other hand, noiseless Vlasov simulations[49–52] that resolve the velocity distribution function on a grid do not inherently have statistical noise to seed parametric instabilities. Fluctuations must, therefore, sometimes be added to the Vlasov simulations in the initial conditions or via an external electric field, to seed any plasma instabilities that are being studied numerically. Fluid simulations can significantly speed up simulations and may be used in weakly nonlinear problems,[14] while kinetic simulations are needed in the nonlinear regime where particle trapping and phase space vortices are important. Reduced kinetic methods combine kinetic and fluid descriptions[53,54] where a full Vlasov kinetic description is maintained only along one "dominant" dimension and fluid moments are taken in the perpendicular dimensions; in fact, the present Vlasov simulation model[55] is in this category, where a kinetic description is used for the momentum in the dimension along the simulation box while the perpendicular momenta have been replaced by the vector potential.

The motivation for the present study is the observation of SRBS in real experiments, in particular, the experimental observations of inflation made in the Trident experiment by Montgomery *et al.*[27] In the Vlasov simulation study by Wang *et al.*,[35] it was shown that SRBS developed in their simulations and they could reproduce the experimental results, if a counter-propagating seed pulse was added in the simulations. We show that our Vlasov code reproduces these results if a resonant seed wave is added. Since no seed wave was used in the Trident experiment, we next introduced random electrostatic noise on thermal level consistent with the fluctuation–dissipation theorem and showed that the SRBS instability still grows in the Vlasov simulations without a seed wave. To verify the Vlasov results with noise, we reproduced them in with a PIC code that produces thermal-like numerical noise self-consistently, and on thermal noise level if the number of computational particles per Debye length fulfills $N_{De} = (2\pi)^2 \lambda_{De}^2 n_e$ with λ_{De} being the electron Debye length and n_e the electron number density. We find that our simple noise model for the Vlasov simulation is accurate enough to drive the SRBS on the same time and spatial scales as in the PIC code.

The paper is organized as follows: In Sec. II, the relevant laser parameters and numerical setup are discussed. Section III discusses the thresholds for convective and absolute instabilities. Section IV compares PIC simulations with Vlasov simulations using thermal-like noise to seed the instability. Conditions on the number of computational particles per Debye length needed in 1D PIC simulations and on the amplitude of an externally applied random electric field in the 1D Vlasov simulations to properly simulate thermal noise are derived. The stages and nonlinear saturation of the SRBS instability are discussed. To compare with the previous simulation study by Wang *et al.*,[35] it is confirmed in Sec. V that the present Vlasov simulations reproduces one of the results if using a counter-propagating seed pulse tuned near the resonant frequency for the backscattered laser in the SRBS interaction. Finally, Sec. VI contains a summary and concluding remarks.

II. LASER PARAMETERS AND NUMERICAL SETUP

The numerical study uses parameters consistent with the Trident laser experiment by Montgomery *et al.*[27] as summarized in Table I. The injected laser has linearly polarized light along the y-axis with the vacuum wavelength $\lambda_{vac} = 0.527\ \mu$m, giving the vacuum wave vector

TABLE I. Summary of physical and derived parameters.

Parameter	Value	Parameter	Value
λ_{vac}	$0.527\,\mu$m	n_{crit}	$4.014 \times 10^{27}\,\mathrm{m}^{-3}$
$k_{vac} = 2\pi/\lambda_{vac}$	$11.923 \times 10^{6}\,\mathrm{m}^{-1}$	$n_0 = 0.025\,n_{crit}$	$1.004 \times 10^{26}\,\mathrm{m}^{-3}$
Laser polarization	Linear along y	ω_{pe}	$5.6514 \times 10^{14}\,\mathrm{s}^{-1}$
T_e	0.5 keV	λ_{De}	$0.01659\,\mu$m
v_{Te}	$9.378 \times 10^{6}\,\mathrm{m/s}$	$n_0\lambda_{De}^3$	458
$\omega_0 = ck_{vac}$	$3.574 \times 10^{15}\,\mathrm{s}^{-1}$	k_0	$11.77 \times 10^{6}\,\mathrm{m}^{-1}$
ω_1	$2.883 \times 10^{15}\,\mathrm{s}^{-1}$	k_1	$-9.430 \times 10^{6}\,\mathrm{m}^{-1}$
ω_L	$6.913 \times 10^{14}\,\mathrm{s}^{-1}$	k_L	$21.20 \times 10^{6}\,\mathrm{m}^{-1}$
γ_L, ν_L	$2.221 \times 10^{13}\,\mathrm{s}^{-1}$	u_{gL}	$8.09 \times 10^{6}\,\mathrm{m/s}$
ν_{ei}	$9.57 \times 10^{11}\,\mathrm{s}^{-1}$	u_{g1}	$2.94 \times 10^{8}\,\mathrm{m/s}$
ν_1	$1.20 \times 10^{10}\,\mathrm{s}^{-1}$	$u_{ph,L} = \omega_L/k_L$	$3.26 \times 10^{7}\,\mathrm{m/s}$
$\gamma_{0,conv}$	$5.155 \times 10^{11}\,\mathrm{s}^{-1}$	$a_{0,conv}$	8.10×10^{-4}
$\gamma_{0,abs}$	$6.694 \times 10^{13}\,\mathrm{s}^{-1}$	$a_{0,abs}$	0.105
L_x	$120\,\mu$m	L_{pl}	$90\,\mu$m

$k_{vac} = 2\pi/\lambda_{vac} = 11.923 \times 10^{6}\,\mathrm{m}^{-1}$ and the angular wave frequency $\omega_0 = ck_{vac} = 3.574 \times 10^{15}\,\mathrm{s}^{-1}$. The equilibrium electron number density in the plasma slab is $n_0 = 0.025 n_{crit} = 1.004 \times 10^{26}\,\mathrm{m}^{-3}$ with $n_{crit} = \epsilon_0 m_e \omega_0^2/e^2 = 4.014 \times 10^{27}\mathrm{m}^{-3}$ being the critical density; hence, the plasma frequency $\omega_{pe} = \sqrt{e^2 n_0/(\epsilon_0 m_e)} = 5.6514 \times 10^{14}\,\mathrm{s}^{-1}$.

Vlasov simulations based on the code described by Eliasson *et al.*[55] and Liu *et al.*[9] and PIC simulations using the Epoch code[56,57] are carried out. The 1D simulation box covers $0 \le x \le L_x$ with $L_x = 140\,\mu$m being the size of the simulation domain and is resolved by 20 000 grid cells, giving a grid size $\Delta x = 7 \times 10^{-3}\,\mu$m. With a Debye length of $\lambda_{De} = \sqrt{\epsilon_0 k_B T_e/n_e e^2} = 0.016\,59\,\mu$m, this corresponds to 2.38 cells per Debye length. The laser pump wave is injected at the left boundary, and light and particles reaching the right or left boundaries are absorbed. The amplitude of the injected laser is kept constant throughout the simulations. To avoid significant interaction between the plasma particles and the spatial boundaries, the plasma particles are initiated sufficiently far away from the boundaries. Thus, the plasma slab of width $L_{pl} = 90\,\mu$m is centered in the middle of the larger ($L_x = 140\,\mu$m) simulation domain. In this way, the laser light has regions with no (or only few) particles near the boundaries when both entering and exiting the simulation domain.

The ions are assumed to form a stationary neutralizing background on the short time scale of the simulations, while the electrons are initially Maxwell distributed with temperature $T_e = 0.5$ keV, giving the electron thermal speed $v_{Te} = \sqrt{k_B T_e/m_e} = 9.378 \times 10^{6}\,\mathrm{m/s}$. This is achieved by initializing the initial electromagnetic fields equal to zero and using only mobile electrons. Since we do not resolve mobile carriers of positive charge and set $E_x(x, t = 0) = 0$, the charge density distribution of all electrons is balanced at each position by a static positive charge (ion) of equal magnitude.

In the PIC simulations, the electrons are resolved by a total of 10^8 computational particles (CPs) corresponding to about 7.8×10^3 CPs per cell and 18.5×10^3 CPs per Debye length, which may give numerical noise on the same level as real thermal noise, as discussed in Sec. IV B. The electrons are initialized with a uniform number density equal to n_0 in the interval $25\,\mu\mathrm{m} \le x \le 115\,\mu$m and zero outside the interval. The time step taken is $\Delta t \approx 0.08\,\omega_0^{-1} = 2.24 \times 10^{-17}$ s. In the Vlasov simulations,[55] the number of momentum dimensions are reduced from three to one by using the conservation of the electron canonical momenta $P_y = p_y - eA_y$ and $P_z = p_z - eA_z$, where A_y and A_z are components of the vector potential. Setting P_y and P_z to zero allows to eliminate the y and z components of the momentum space by assuming that the thermal motion of the electrons perpendicular to the laser propagation direction does not have significant impact of the dynamics. The ponderomotive force on the electrons (due to the nonlinear $\mathbf{v} \times \mathbf{B}$ force in the laser field) is then obtained as $F_{p,x} = -m_e c^2 \partial\gamma/\partial x$, where $\gamma = \sqrt{1 + (p_x^2 + e^2A_y^2 + e^2A_z^2)/m_e^2c^2}$ is the relativistic gamma factor. The electron momentum space has numerical boundaries at $\pm 0.4 m_e c$, where the distribution function is set to zero, and is resolved by 1200 grid cells in momentum space; the boundaries are chosen at high enough momentum values such that accelerated electrons (cf. Fig. 3) do not reach the boundaries. The functional form of the initial electron number density in the Vlasov simulations is $n_e(x, t = 0) = n_0(1 + \tanh\{[x - (L_x - L_{pl})/2]/D_{ramp}\}) \times (1 - \tanh\{[x - (L_x + L_{pl})/2]/D_{ramp}\})/4$ with the ramp $D_{ramp} = 50k_{vac}^{-1}$. The Vlasov simulations use the time step $\Delta t = 0.1\,\omega_0^{-1} = 2.80 \times 10^{-17}$ s. In addition, it is necessary to use a mild numerical dissipation in the numerical approximation of the Vlasov equation to avoid aliasing effects in space when electrons start to get trapped in the electrostatic potential of the large amplitude Langmuir wave, in addition to the so-called recurrence effect due to phase mixing in momentum space.[58–60] In the Vlasov simulations, we are adding a diffusion term (calculated using centered difference approximations) as $D(f_e) = 0.005|p|(\partial^2 f_e/\partial x^2)\Delta x/m_e + 0.00125(\partial^2 f_e/\partial p^2)e|E_x|\Delta p$, which is large enough to prevent numerical heating but small enough not to influence the physics significantly.

For the electrostatic waves, the main damping mechanism is Landau damping, $\nu_L = \gamma_L$, while for the electromagnetic sideband the damping is due to electron-ion collisions, $\nu_1 = 0.5\nu_{ei}\omega_{pe}^2/\omega_1^2$,[61] where the electron–ion collision frequency is estimated as $\nu_{ei} = 3\omega_{pe}\log(\Lambda)/\Lambda$ with $\Lambda = 12\pi n_0 \lambda_{De}^3$.[62] In the Vlasov simulations, a simple Bhatnagar–Gross–Krook (BGK) collision operator $(\partial f/\partial t)_{coll} = \nu_{ei}^{kin}(p_x)(f_0(x, p_x) - f_e(x, p_x, t))$ is used, where $f_0(x, p_x)$ is the initial electron distribution function, and with the velocity-dependent collision frequency $\nu_{ei}^{kin} = 3\omega_{pe}\log(\tilde{\Lambda})/\tilde{\Lambda}$ with $\tilde{\Lambda} = 12\pi n_0 u^3/\omega_{pe}^3$ and $u = (v_{Te}^2 + p_x^2/m_e^2)^{1/2}$, supporting the decrease in the Coulomb collision frequency for high energy electrons. The BGK collision operator does not conserve energy and particles exactly, but this effect is relatively small in the rapidly oscillating fields. A damping of the electromagnetic (EM) wave is introduced in the Vlasov simulations with rate $\nu_{EM} = 0.5\nu_{ei}\omega_{pe}^2/\omega_0^2$, via a simple friction term in the EM wave equation for the vector potential as $\partial^2\mathbf{A}/\partial t^2 + \nu_{EM}\partial\mathbf{A}/\partial t - c^2\partial^2\mathbf{A}/\partial x^2 + \Omega_p^2\mathbf{A} = 0$, where Ω_p is the relativistically corrected plasma frequency (see more details in Ref. 55). It should be noted that the electron–ion collision frequency ν_{ei} is about 23 times smaller than the linear Landau damping rate (cf. Table I), and therefore, damping due to collisions is relatively unimportant. The damping rate of the EM wave due to electron-ion collisions is also very small due to the low plasma density. No significant effects due to collisions were seen in the Vlasov simulations, and therefore, the built-in modules

for collisions were not activated in the Epoch code[56,57] for the PIC simulations.

III. CONVECTIVE AND ABSOLUTE SRBS INSTABILITY

The SRBS interaction is governed by the matching conditions $\omega_1 = \omega_0 - \omega_L$ and $k_L = k_0 - k_1$, with (ω_0, k_0) being the frequency and wave vector of the pump wave, (ω_1, k_1) of the backscattered sideband, and (ω_L, k_L) of the Langmuir wave. Each mode obeys its respective linear dispersion relation, so that $k_0 = k_{vac}\sqrt{(\omega_0^2 - \omega_{pe}^2)/\omega_0^2}$, $k_1 = -k_{vac}\sqrt{(\omega_1^2 - \omega_{pe}^2)/\omega_0^2}$, and the real ω_L is obtained for a given k_L through the kinetic dispersion relation $\varepsilon_L(k_L, \omega_L) = 0$ for Langmuir waves with the dielectric constant ε_L in Eq. (10) derived from linearized Vlasov theory with Maxwell distributed electrons. Assuming real-valued wave vectors k_L and complex-valued frequencies $\omega_L = \omega_{L,R} + i\omega_{L,R}$, the solution of $\varepsilon_L(k_L, \omega_L) = 0$ gives the resonant wave vector $k_L = 0.3518\lambda_{De}^{-1}$ where $\lambda_{De} = \sqrt{\epsilon_0 k_B T_e/n_e e^2}$ is the electron Debye length, and the real-valued Langmuir wave frequency $\omega_L \approx \omega_{L,R} = 1.2233\,\omega_{pe}$, as well as the Landau damping rate $\gamma_L = -\omega_{L,I} = 0.0353\,\omega_{pe}$. The resonant wavenumbers and frequencies are listed in Table I.

A mode coupling model for the Langmuir and scattered laser daughter waves a_L and a_1[63] is given as

$$\frac{\partial a_L}{\partial t} + \nu_L a_L + u_{gL}\frac{\partial a_L}{\partial x} = \gamma_0 a_1, \tag{1}$$

$$\frac{\partial a_1}{\partial t} + \nu_1 a_1 - u_{g1}\frac{\partial a_1}{\partial x} = \gamma_0 a_L, \tag{2}$$

where ν_L and ν_1 are the respective damping rates, $\gamma_0 = (\omega_{pe}^2/\omega_L\omega_1)^{1/2} \times k_L u_0/4$ corresponds to the growth rate of the SRBS instability in an infinite homogeneous plasma in the absence of damping, and $u_0 = eE_0/m_e\omega_0$ is the quiver velocity of an electron in the laser electric field of amplitude E_0. The normalized amplitude is defined as $a_0 = u_0/c = eE_0/m_e\omega_0 c$, giving the linear relationship $\gamma_0 = (\omega_{pe}^2/\omega_L\omega_1)^{1/2} \times (k_L c/4)a_0$ between (γ_0, a_0) and similarly between $(\gamma_{0,conv}, a_{0,conv})$ and $(\gamma_{0,abs}, a_{0,abs})$ as discussed below and given in Table I. Furthermore, the group velocities of the Langmuir and electromagnetic daughter waves are $u_{gL} = \partial\omega_L/\partial k_L = 3v_{Te}^2 k_L/\omega_L$ (obtained from the Bohm–Gross dispersion relation $\omega_L^2 = \omega_{pe}^2 + 3v_{Te}^2 k_L^2$) and $u_1 = \partial\omega_1/\partial k_1 = c^2 k_1/\omega_1$. In deriving Eqs. (1) and (2), the amplitudes of the oppositely propagating waves have been written $A_{L,1} = a_{L,1}(x,t)\exp(ik_{L,1}x - i\omega_{L,1}t)$, and it is assumed that the envelopes $a_{L,1}(x,t)$ vary slowly in space and time compared to $\exp(ik_{L,1}x - i\omega_{L,1}t)$. The threshold amplitude for the convective instability is

$$\gamma_0 > \gamma_{0,conv} \equiv \sqrt{\nu_L\nu_1}, \tag{3}$$

while an absolute instability takes place for[9,63,64]

$$\gamma_0 > \gamma_{0,abs} \equiv \frac{1}{2}\sqrt{u_{gL}u_{g1}}(\kappa_L + \kappa_1), \tag{4}$$

as obtained using the saddle-point method, where $\kappa_L = \nu_L/u_{gL}$ and $\kappa_1 = \nu_1/u_{g1}$. The thresholds for absolute and convective instabilities (3) and (4) are related through

$$\gamma_{0,abs} = \frac{1}{2}(s^{1/2} + s^{-1/2})\gamma_{0,conv}, \tag{5}$$

with $s = (\nu_L/\nu_1)(u_{g1}/u_{gL})$, showing that $\gamma_{0,abs} \geq \gamma_{0,conv}$ since the multiplying factor on the right-hand side of Eq. (5) has the minimum 1 for $s = 1$; the parameters in Table I gives $s = 6.7 \times 10^4 \gg 1$ and, therefore, $\gamma_{0,abs} \approx (s^{1/2}/2)\gamma_{0,conv} = \left(\nu_L\sqrt{u_{g1}/u_{gL}}\right)/2$. The convective instability [$\propto \exp(-\kappa_{conv}x)$, increasing toward negative x] for $\gamma_0 > \gamma_{0,conv}$ has the spatial growth rate

$$\kappa_{conv} = \frac{\kappa_L - \kappa_1}{2} - \sqrt{\frac{(\kappa_L - \kappa_1)^2}{4} + \frac{\gamma_{0,conv}^2 - \gamma_0^2}{u_{gL}u_{g1}}} \tag{6}$$

for $\gamma_0 > \gamma_{0,conv}$, and which vanishes as $\gamma_0 \to \gamma_{0,conv}$. For $\nu_L/u_{gL} \gg \nu_1/u_{g1}$ and $\gamma_0^2 \gg \gamma_{0,conv}^2$, one has $\kappa_{conv} \approx \gamma_0^2/\nu_L u_{g1}$.[2,65] The absolute instability [$\propto \exp(\gamma_{abs}t)$] for $\gamma_0 > \gamma_{0,abs}$ has the temporal growth rate

$$\gamma_{abs} = \frac{2(\gamma_0 - \gamma_{0,abs})}{\sqrt{u_{g1}/u_{gL}} + \sqrt{u_{gL}/u_{g1}}}. \tag{7}$$

For our numerical study, we use the laser intensities $I_0 = c\epsilon_0 E_0^2/2$ and corresponding normalized amplitudes $a_0 = eE_0/m_e\omega_0 c$ given in Table II. The values of a_0 are all below the threshold $a_{0,abs}$ for absolute instability but above $a_{0,conv}$ of the convective instability given in Table I. For the size of the plasma slab, $L_{pl} = 90\,\mu$m, the number of e-foldings (amplitude gain) $\kappa_{conv}L_{pl}$ is about 3.4, 2.3, and 1.3 for $a_0 = 0.0246$, 0.020, and 0.015, respectively, corresponding to exponential amplification factors $\exp(\kappa_{conv}L_{pl})$ of 31, 10, and 3.5, with which thermal emissions in the plasma will be amplified. Since the gain is inversely proportional to the electron (collisional + Landau damping) rate, a moderate decrease in the Landau damping rate may lead to a significant (exponential) increase in the amplification factor.

IV. RANDOM FLUCTUATIONS IN VLASOV AND PIC SIMULATIONS

The theory of thermal fluctuations in plasma is here briefly reviewed, and how these fluctuations are related to numerical noise in 1D PIC and Vlasov simulations.

A. Thermal fluctuations in plasmas

Thermal fluctuations may be estimated from spontaneous emissions of electrostatic waves as a consequence of the fluctuation–dissipation theorem, giving the average square of the fluctuating electrostatic electric field,[38–41]

TABLE II. Convective growth vs laser intensity.

I_0(W/cm^2)	E_0 (V/m)	a_0	κ_{conv} (m^{-1})	$\kappa_{conv}L_{pl}$	exp $(\kappa_{conv}L_{pl})$
3.0×10^{15}	1.50×10^{11}	0.0246	38.2×10^3	3.4	31
2.0×10^{15}	1.23×10^{11}	0.020	25.3×10^3	2.3	10
1.1×10^{15}	0.91×10^{11}	0.015	13.9×10^3	1.3	3.5

$$\langle E^2(\mathbf{r},t)\rangle = \int\int W^{3D}(k,\omega)\, d^3k\, d\omega, \tag{8}$$

where $W^{3D}(k,\omega)$ is the spectral power density of the electrostatic electric field fluctuations, and we denoted $k = |\mathbf{k}|$ using that the spectrum is isotropic in the absence of a guiding magnetic field. For Maxwell distributed electrons, neglecting the contributions from the ions, the spectral density can be written as

$$W^{3D}(k,\omega) = -\frac{2}{(2\pi)^4}\frac{k_B T_e}{\omega\epsilon_0}\Im\left(\frac{1}{\varepsilon_L}\right), \tag{9}$$

where $\Im$ denotes the imaginary part and $\varepsilon_L(k,\omega)$ is the dielectric function of the longitudinal electron fluctuations, which is given by

$$\varepsilon_L = 1 + \frac{\omega_{pe}^2}{k^2 v_{Te}^2}[1 + \xi_e Z(\xi_e)], \tag{10}$$

where $\xi_e = \omega/\left(\sqrt{2}kv_{Te}\right)$ and $Z(\xi) = i\sqrt{\pi}e^{-\xi^2} - 2w_D(\xi)$ is the plasma dispersion function[66] with

$$w_D(\xi) = e^{-\xi^2}\int_0^\xi e^{t^2}dt \tag{11}$$

being Dawson's integral.[67–69]

The theoretical thermal noise spectrum (9) is plotted in Fig. 1. The Langmuir wave branch shown by a curve is obtained by solving $\varepsilon_L = 0$ for real k and complex-valued ω and by plotting the real part of ω. Equation (9) is not exactly singular along the curve, because real-valued ω and $\mathbf{k}$ are used as input in ε_L, which then becomes complex-valued and non-zero due to the complex term $i\sqrt{\pi}e^{-\xi^2}$ in the plasma dispersion function. However, in the white area for small wavenumbers in Fig. 1, the Landau resonance term becomes very small and Eq. (9) becomes *almost* singular along the curve for weakly Landau damped Langmuir waves. The spectrum shows enhanced fluctuations around the Langmuir wave branch, and a broad diffuse spectrum due to the Maxwell distributed free-streaming electrons for $\omega/k \le 3v_{Te}$; for $\omega/k \gg 3v_{Te}$, there are only few electrons contributing to the fluctuations and the spectrum vanishes except at the Langmuir wave branch ($\omega \approx \omega_{pe}$), where $W^{3D}(k,\omega)$ becomes delta function-like for $k \ll \lambda_{De}^{-1}$. For $k > \lambda_{De}^{-1}$, the oscillations are strongly Landau damped, providing a natural cutoff of the integration. More careful considerations using kinetic theory involving close collisions are given by Dawson and Oberman.[70]

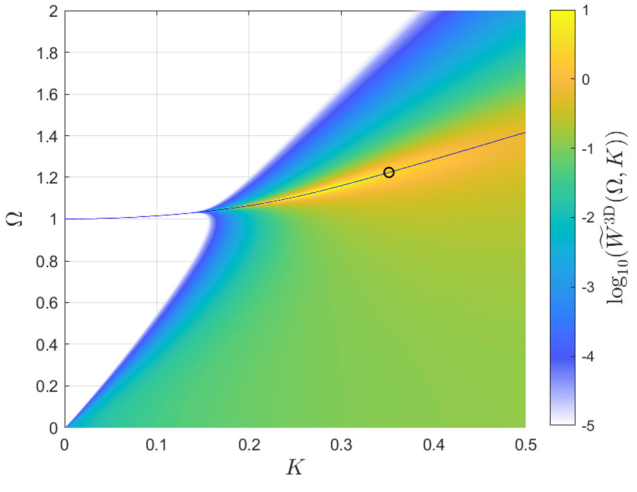

FIG. 1. (a) Theoretical noise spectrum of electrostatic fluctuations for Maxwell distributed electrons, in logarithmic scale $\log_{10}(\tilde{W}^{3D}(\Omega,K))$, where the normalized spectrum $\tilde{W}^{3D}(\Omega,K) = (2\pi)^3\epsilon_0 W^{3D}(\omega,k)\omega_{pe}/k_B T_e$ with normalized wavenumber $K = \lambda_{De}k$ and frequency $\Omega = \omega/\omega_{pe}$. The curve indicates the real part of ω from the dispersion relation $\varepsilon_L(\omega,k) = 0$ and the ring the resonant Langmuir wave $(\omega,k) = (\omega_L, k_L)$ in the Raman interaction.

B. Fluctuations in 1D PIC and Vlasov simulations

It is interesting to note that even though PIC simulations, in general, aim to approximate the continuous Vlasov equation that explicitly excludes thermal fluctuations,[40] the computational particles lead to a graininess of the velocity distribution function resulting in numerical noise.[46,47] Dieckmann *et al.*[48] demonstrated that PIC simulations indeed produce simulation noise spectra qualitatively similar to the thermal noise spectrum in Fig. 1.

In preparation for PIC and Vlasov simulations, we derive the spectrum for a one-dimensional (1D) geometry in space. In 1D PIC and Vlasov simulations, the computational particles and spatial perturbations are assumed to extend indefinitely in two of the spatial dimensions. A 1D spectrum can in principle be obtained by integrating the three-dimensional (3D) spectral density over two of the vector components (k_y and k_z). However, with the knowledge that wave modes are strongly Landau damped for $k > \lambda_{De}^{-1}$, we instead for simplicity evaluate the 3D spectral density at $(k,\omega) = (k_x,\omega)$ and multiply the result by λ_{De}^{-2} to obtain a 1D spectral density,

$$W^{1D}(k_x,\omega) \approx W^{3D}(k_x,\omega)\lambda_{De}^{-2}. \tag{12}$$

On the other hand, assuming from the outset a purely 1D geometry in the x-dimension in the test particle approach,[40] the test particle is a point-particle in the x-direction but extends indefinitely in the y- and z-directions, effectively forming a moving infinitely wide charged "plate." Assuming that the test "particle" has surface charge density ρ^{2D} (Coulombs per m^2) in the y-z plane and assuming a 1D number density of n_e^{1D} test particles per unit length, the spectral density for Maxwell distributed electrons can with the test particle approach be derived as (cf. the Appendix)

$$W^{1D}(k_x,\omega) = -\frac{2}{(2\pi)^2}\frac{k_B T_e}{\omega\epsilon_0}\frac{(\rho^{2D})^2 n_e^{1D}}{\epsilon_0 m_e\omega_{pe}^2}\Im\left(\frac{1}{\varepsilon_L}\right), \tag{13}$$

with the mean squared electric field being

$$\langle E^2\rangle = \int\int W^{1D}(k_x,\omega)\, dk_x\, d\omega. \tag{14}$$

We denote $\rho^{2D} = en_e^{2D}$ where n_e^{2D} represents the surface number density. Then, $n_e = n_e^{2D}n_e^{1D}$ is the volume number density of electrons. Inserting $\rho^{2D} = en_e^{2D} = en_e/n_e^{1D}$ into Eq. (13) and using Eq. (9) gives

$$W^{1D}(k_x,\omega) = -\frac{n_e}{n_e^{1D}}\frac{2}{(2\pi)^2}\frac{k_B T_e}{\omega\epsilon_0}\Im\left(\frac{1}{\epsilon_L}\right) = (2\pi)^2\frac{n_e}{n_e^{1D}}W^{3D}(k_x,\omega). \tag{15}$$

Equating Eqs. (12) and (15) gives $n_e^{1D} = (2\pi)^2 \lambda_{De}^2 n_e$, corresponding to the number of particles per Debye length $N_{De} = \lambda_{De} n_e^{1D} = (2\pi)^2 \lambda_{De}^3 n_e$. Using that the plasma parameter $\lambda_{De}^3 n_e = 458$ (cf. Table I), we have $N_{De} = 18 \times 10^3$, and for the used plasma size $L_{pl} = 90\,\mu\text{m} = 5500\lambda_{De}$, we have the total number of test particles $N_{tot} = 5500 N_{De} \approx 10^8$. In the 1D PIC simulation presented below, we have used the same number of computational particles per Debye length as N_{De} to keep the numerical noise on the same order of magnitude level as real thermal noise. The Epoch code uses triangular shape functions (cf. the Appendix) which in Fourier space results in a multiplication of the spectral density by the Fourier transformed shape function squared, $|\hat{S}(k)|^2 = \sin^4(kD)/(kD)^4$, where $D = \Delta x/2 \approx 0.21\,\lambda_{De}$. The shape function decreases the spectral density only for large k, and to decrease the spectral density by 10% would require $k\lambda_{De} \gtrsim 2$ which is 5–6 times larger than the wavenumbers of the resonant Langmuir wave (cf. Fig. 1).

To imitate thermal fluctuations in the Vlasov simulation, we introduce an external electrostatic field E_{ext} on the grid points in space and time, with the random values of E_{ext} uniformly distributed in the range $[-E_{rand}, E_{rand}]$. The amplitudes are on average uniformly distributed on the Fourier components (ω, k_x) up to the respective Nyquist limits $(\pm\pi/\Delta t, \pm\pi/\Delta x)$ with a spatiotemporal spectral density having the constant value

$$W_{ext}^{1D}(\omega, k_x) = \frac{E_{rand}^2}{3} \frac{\Delta x}{2\pi} \frac{\Delta t}{2\pi}, \tag{16}$$

where Δx and Δt are the grid sizes in space and time. Here, $E_{rand}^2/3$ is the mean squared amplitude of the uniform random electric field values, and $2\pi/\Delta x\ 2\pi/\Delta t$ represent the widths of the spectral densities in wavenumber and frequency space. The amplitude of the external electric field fluctuations needs to be calibrated such that the self-consistent electric field fluctuations in the Vlasov simulations have the same spectral density as thermal noise in Fig. 1 around the resonant frequency and wavenumber (ω_L, k_L). Setting

$$W_{ext}^{1D} = \alpha W^{1D}(\omega_L, k_L) \tag{17}$$

with the calibration parameter α being a relative spectral density of the external fluctuations, the random electric field amplitude E_{rand} is determined as

$$E_{rand} = \sqrt{3 \frac{2\pi}{\Delta x} \frac{2\pi}{\Delta t} \alpha W^{1D}(\omega_L, k_L)}. \tag{18}$$

In Fig. 1, it is seen that $(2\pi)^3 \epsilon_0 W^{3D}(\omega_L, k_L) \omega_{pe}/k_B T_e \approx 1$ at the resonant frequency and wavenumber (indicated by a ring), so that the 1D spectral density $W^{1D}(\omega_L, k_L) \approx k_B T_e/((2\pi)^3 \epsilon_0 \omega_{pe} \lambda_{De}^2)$, giving the random electric field amplitude

$$E_{rand} = \sqrt{3 \frac{2\pi}{\Delta x} \frac{2\pi}{\Delta t} \frac{\alpha k_B T_e}{(2\pi)^3 \epsilon_0 \omega_{pe} \lambda_{De}^2}} = \sqrt{\frac{3\alpha}{2\pi} \frac{\omega_{pe} m_e}{\Delta x \Delta t \epsilon_0}}. \tag{19}$$

We recall that the used grid sizes in space and time are $\Delta x = 7 \times 10^{-9}$ m and $\Delta t = 2.80 \times 10^{-17}$ s, giving the normalized amplitude $eE_{rand}/\omega_0 m_e c \approx 0.002\sqrt{\alpha}$. For a low-amplitude external electric field injected at the resonant wavenumber and frequency (ω_L, k_L), it is found in a Vlasov simulation without laser (not shown) that the amplitude of the external electrostatic field is amplified about 16 times, corresponding to a power amplification of 256 times. A noise level near the predicted amplitude of the thermal noise at the resonant Langmuir wave, therefore, corresponds to $\alpha = 1/256 \approx 0.004$ and $eE_{rand}/\omega_0 m_e c \approx 1.25 \times 10^{-4}$.

V. SIMULATION RESULTS

Vlasov and PIC simulations are carried out to compare the effects of externally injected noise in the Vlasov simulations and numerical noise in the PIC simulations on the Raman backscattering instability.

A. Vlasov simulation with added noise

Vlasov simulations are carried out with normalized injected laser amplitude $a_0 = eE_0/m_e\omega_0 c = 0.0246$, corresponding to an intensity $I_0 = c\epsilon_0 E_0^2/2 = 3 \times 10^{15}\,\text{W/cm}^2$ (cf. Table II). Figure 2 shows the spatiotemporal evolution of the backscattered light and electrostatic fluctuations using different values of the relative spectral density α of the external noise. The backscattered light is obtained from the solution by Fourier transforming the wave EM field and keeping only components with negative wavenumbers. The case $\alpha = 0.004$, corresponding to thermal noise level, is shown in Figs. 2(a) and 2(b). For times $\omega_0 t < 10^4$, the convective instability is of low amplitude, followed by visible backscattered light for $\omega_0 t > 10^4$ with an amplitude maximum near the left boundary. Electrostatic waves [Fig. 2(b)] are propagating into the domain with a velocity comparable to the phase velocity $u_{ph,L} = \omega_L/k_L = 0.11c$ of the resonant Langmuir wave. Large amplitude pulses of reflected light are excited at $\omega_0 t = 2 \times 10^4$ and 2.4×10^4. Similar results are obtained by larger fluctuation levels $\alpha = 0.016$ [Figs. 2(c) and 2(d)] and 0.064 [Figs. 2(e) and 2(f)] with the convective instability being visible slightly earlier, at $\omega_0 t \gtrsim 0.7 \times 10^4$. The normalized amplitudes of the backscattered lights in Figs. 2(a), 2(c), and 2(e) are in the range $a \sim 0.005 - 0.009$, which compared to the injected amplitude $a_0 = 0.0246$ gives a reflectivity $a^2/a_0^2 \sim 4\% - 13\%$, which is comparable with the observed peak reflectivities $5\% - 10\%$ in the experiment by Montgomery *et al.*[27] as shown in their Fig. 5. However, for $\alpha = 0.25$ [Figs. 2(g) and 2(h)], the large amplitude random fluctuations wash out the three-wave Raman interaction and there is only weak scattering off the fluctuations but no signature of SRBS instability. Also, in the absence of random fluctuations with $\alpha = 0$ (not shown), there is no sign of instability within the simulation time.

The initial evolution of the electron distribution function in Figs. 2(a) and 2(b) for $\omega_0 t < 10^4$ may be governed by quasi-linear evolution in which the resonantly driven Langmuir wave is linearly Landau damped and a plateau is formed in the background electron velocity distribution function. The SRBS instability excites a narrow spectrum of Langmuir waves, which on average may introduce a diffusion of the electron distribution function in velocity/momentum space. The slow evolution of the average electron velocity distribution function $F_e(v_x, t) = \langle f_e \rangle$ is then described by a Fokker–Planck equation,[71]

$$\frac{\partial F_e}{\partial t} = \frac{\partial}{\partial v_x} \left(D \frac{\partial F_e}{\partial v_x} \right) \tag{20}$$

with $v_x \approx p_x/m_e$ for weakly relativistic electrons and where the diffusion coefficient is given by

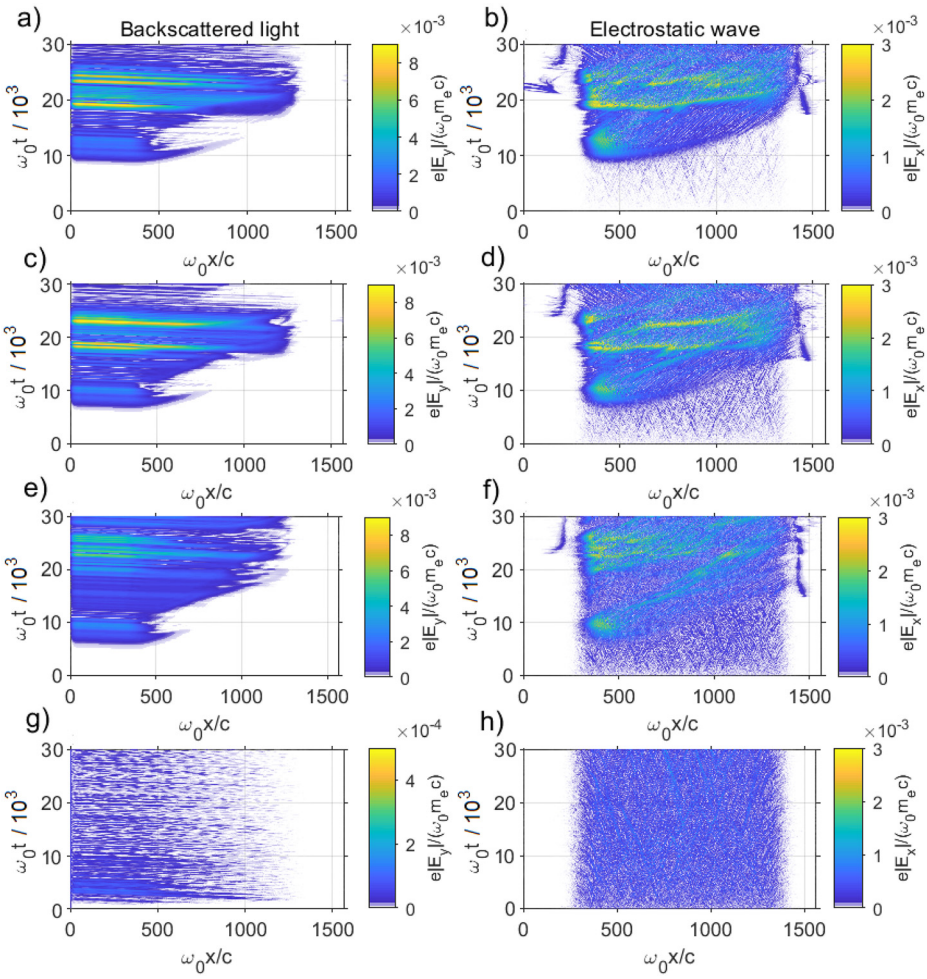

FIG. 2. Vlasov simulation results showing the normalized amplitude of the backscattered laser light (left column) and electrostatic waves (right column) for different levels of external noise with (a) and (b) $\alpha = 0.004$, (c) and (d) $\alpha = 0.016$, (e) and (f) $\alpha = 0.064$, and (g) and (h) $\alpha = 0.250$. The normalized laser amplitude is $a_0 = 0.0246$ for all cases.

$$D(v_x) = \frac{\pi e^2}{m_e^2} \frac{W(k_x)_{k_x=\omega_L/v_x}}{|v_x|} \tag{21}$$

and $W(k_x) = \Delta E_x^2/\Delta k_x$ is the spectral density of the Langmuir electric field per differential wavenumber Δk_x, with ΔE_x^2 being the differential squared electric field. For enhanced fluctuations near the frequency and wavenumber of the resonantly excited Langmuir wave, the wave spectrum and diffusion coefficient will become strongly peaked near the phase velocity $u_{ph,L} = \omega_L/k_L$. The quasilinear evolution model governs the scattering of electrons by a spectrum of waves, but does not take into account the nonlinear stage with trapping of electrons in the wave potential, and is, therefore, justified only in the very initial stage of the convective SRBS instability.

Figure 3 shows snapshots in time of the averaged and non-averaged perturbed electron distribution function $\Delta f_e = f_e - f_{e0}$. The averaging procedure involves first taking the average of Δf_e evaluated at four times t, $t - \Delta t_{dump}$, $t - 2\Delta t_{dump}$, and $t - 3\Delta t_{dump}$, where $\Delta t_{dump} = 100\,\omega_0^{-1}$. After this, the result is Fourier transformed in space and only the 10 lowest Fourier components are kept. In this fashion, rapid oscillations in space and time are strongly reduced in the averaged perturbed electron distribution function. It is seen in Fig. 3(a) at $\omega_0 t = 5000$ that the averaged distribution function is modified in a narrow band near the resonant velocity leading to a plateau in the electron distribution function. The non-averaged distribution function in Fig. 3(g) shows the initial scattering of electrons by the Langmuir wave potential into an accelerated population of electrons. The plateau is convected into the spatial domain with a velocity comparable to the resonant phase velocity $u_{ph,L} = \omega_L/k_L$ until a large portion of the plasma slab contain a plateau in the electron distribution function; a narrow flat region in velocity leads to a significant decrease in the Landau damping.[72] As the Landau damping rate $\propto \partial f_e/\partial v$ at $v = u_{ph,L}$ decreases with time, the growth rate of the convective SRBS instability increases, and at $\omega_0 t \approx 10^4$, the Langmuir waves near the left boundary has become large enough amplitude to trap a significant portion electrons [Fig. 3(i)] which on average lead to a flat-topped distribution function [Fig. 3(c)], convecting from left to right into the domain interior. The periodic phase space holes with trapped electrons in Fig. 3(i) undergoes trapped particle merging instabilities[73–75] where adjacent electron holes merge, cascading to longer wavelengths, resulting in turbulent Langmuir waves in Fig. 3(j) and a resulting flattening of the electron distribution function in the interior of the domain in Figs. 3(e) and 3(k). This is also seen and discussed for the PIC

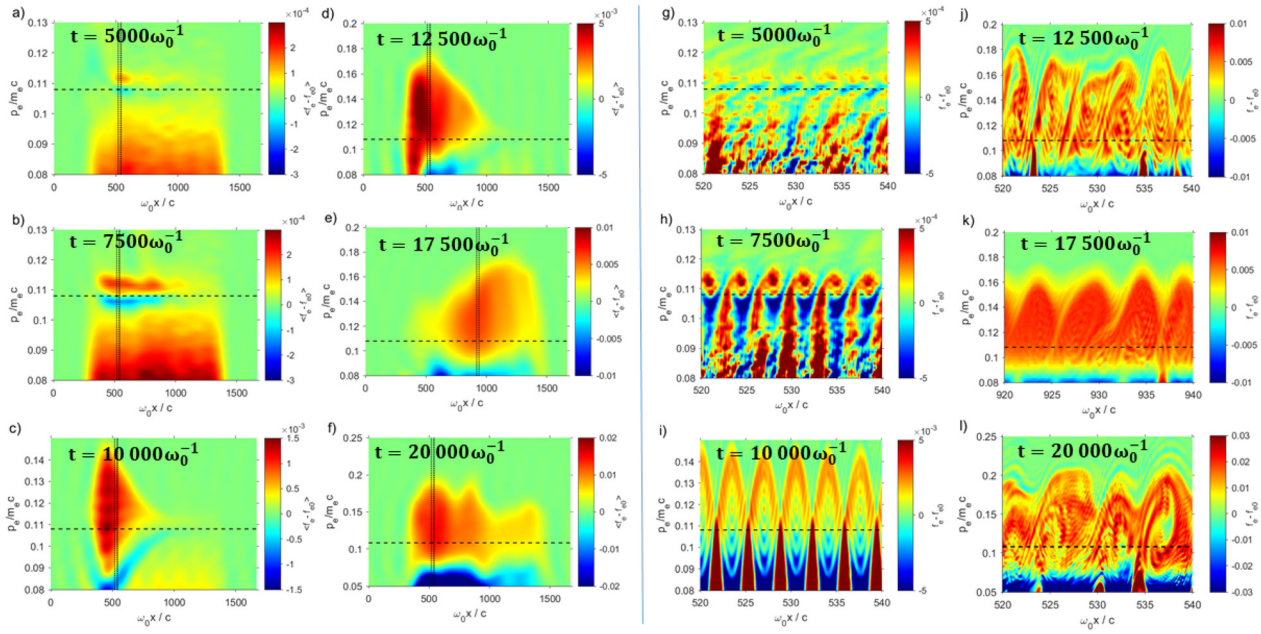

FIG. 3. (a)–(f) Vlasov simulation showing the averaged momentum distribution function $F_e = \langle \Delta f_e \rangle$ at different times as indicated in each panel, with $\Delta f_e = f_e - f_{e0}$ being the perturbed electron distribution function. (g)–(l) Close-ups of the non-averaged distribution function Δf_e in regions indicated by pairs of vertical dotted lines in (a)–(f). The resonant Langmuir wave phase speed $u_{ph,L} = \omega_L/k_L = 0.11\,c$ is indicated by horizontal dashed lines in all panels. Same simulation as in Figs. 2(a) and 2(b) using $a_0 = 0.0246$ and $\alpha = 0.004$. See movies in the supplementary material showing the dynamics of the electron distribution function.

simulation in Fig. 5. A second phase in Fig. 3 occurs at $\omega_0 t \approx 2 \times 10^4$ when the flattened electron distribution function covers a large part of the domain, leading to weakly Landau damped electrostatic waves. At this time, the laser undergoes a second phase of inflationary growth of the instability with a signature of absolute instability, in a process described by Wang *et al.*[35] Peaks in the backscattered light is seen in Fig. 2(a) also at $\omega_0 t \approx 2.4 \times 10^4$, correlated with large amplitude electrostatic waves in Fig. 2(b) [and similarly for Figs. 2(c) and 2(d)]. This corresponds to where the flattened distribution function leads to that the SRBS instability again can grow to large amplitude. After this stage, the laser light continues to be reflected off large-amplitude Langmuir waves, but at a somewhat lower level because hot electrons have been reflected at the right plasma boundary and fills up the whole domain, and the coherence of the Raman interaction is blurred by the large amplitude plasma turbulence. See movies in the supplementary material showing the dynamics of the electron distribution function.

B. PIC simulation emulating thermal noise

We next carry out a PIC simulation with 10^8 computational particles such that the numerical noise is reduced to thermal noise level (cf. Sec. IV B). We again inject a laser with the intensity $I_0 = 3 \times 10^{15}\,\mathrm{W/cm^2}$ at the left boundary of the PIC simulation box. We advance the simulation in time for $\omega_0 t = 1.6 \times 10^4$ corresponding to about 4.4 ps, resolved by 2.1×10^5 time steps.

Figures 4(a) and 4(e) show the envelopes of the backscattered laser light and of the electrostatic wave, which are excited by the three-wave interaction. We extracted $E_y(x,t)$ of the backscattered light by performing a 2D Fourier transform over the full simulation box and over the time interval $2 \times 10^3 \le \omega_0 t \le 1.6 \times 10^4$. At the time $\omega_0 t = 2 \times 10^3$, the laser pulse has crossed the full simulation box length. By not including the data sampled before this time, we reduce aliasing due to a non-periodic time series. In Fourier space, we set the Fourier components in both quadrants with $\omega/k \ge 0$ to zero. The inverse Fourier transform returns the value of $E_y(x,t)$ of the backscattered wave. In Fig. 4(a), the envelope of the electric field is obtained by calculating the maximum value of $|E_y|$ in a space interval $[x - \delta_x/2, x + \delta_x/2]$ and time interval $[t - \delta_t/2, t + \delta_t/2]$ where $\delta_x = 2.6\,c/\omega_{pe}$ and $\delta_t \approx 8\,\omega_0^{-1}$.

The Fourier spectra of $E_y(x,t)$ for the three separate space-time intervals labeled 1–3 in Figs. 4(a) and 4(e) are shown in Figs. 4(b)–4(d). All three space-time intervals in Figs. 4(a) and 4(e) are $N_x = 12\,820$ cells wide, which equals $L_x = 1070\,c/\omega_0$, and cover $N_t = 10^3$ data time steps over a time interval $L_t = 2000\,\omega_0^{-1}$. The wavenumber and frequency resolutions are $dk = 2\pi/L_x$ and $d\omega = 2\pi/L_t$. The power spectra of $E_y(x,t)$ in Figs. 4(b)–4(d) and $E_x(x,t)$ in Figs. 5(a)–5(c) are normalized to $C_0 = \omega_{pe} k_B T_e N_x^2 N_t^2\, dk\, d\omega/((2\pi)^3 \epsilon_0 v_{Te}^2)$, which is the same normalization as in the thermal noise spectrum in Fig. 1. The linear dispersion relation of the light mode $\omega(k) = (\omega_{pe}^2 + c^2k^2)^{1/2}$ is overplotted in Figs. 4(b)–4(d).

Figure 4(a) shows no visible secondary waves prior to $\omega_0 t = 6000$. This is confirmed by the wave spectrum in box 1 in Fig. 4(b), where a single strong peak is centered at the frequency and wavenumber (ω_0, k_0) of the laser with the phase velocity $\omega/k > 0$. The envelopes of the electric fields of both the laser and electrostatic secondary waves in Figs. 4(a) and 4(e) start to grow visibly after $\omega_0 t = 6500$. The amplitudes of both reach their maxima at around $\omega_0 t \approx 8000$ near the

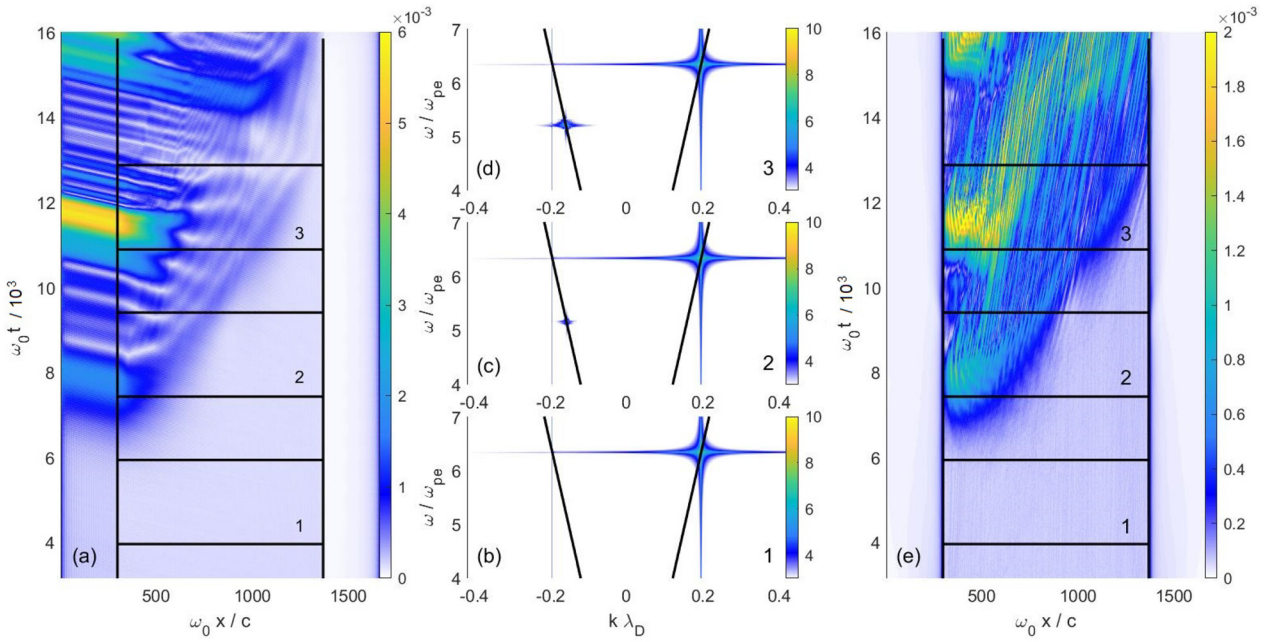

FIG. 4. PIC simulation showing the electric fields of the secondary waves: Panel (a) shows the envelope of the electric E_y component of the backscattered wave. Panels (b)–(d) show the Fourier spectra of $E_y(x,t)$ for the boxes 1, 2, and 3 in (a) and (e). The solution of the dispersion relation of the light mode is overplotted in black. Panel (e) depicts the envelope of the electrostatic field E_x. Vertical lines in (a) and (e) mark the plasma boundaries. Amplitudes in (a) and (e) are normalized to $m_e c\omega_0/e$ and the Fourier spectra to C_0. See the movie showing the dynamics of the system in the supplementary material.

left boundary of the electron plasma. Figure 4(c) reveals a new peak on the light mode in the quadrant $\omega/k < 0$ with the frequency and wavenumber (ω_1, k_1) of the backscattered wave.

Prior to $\omega_0 t = 10^4$, the amplitude of the backscattered light mode remains much below that of the laser field $eE_0/m_e c\omega_0 = 0.0246$ while the spatial interval, in which both secondary waves grow, gradually expands. It ranges from the left boundary of the plasma to about $x\omega_0/c \approx 10^3$ when a major burst of backscattered light erupts. It reaches a peak amplitude close to 20% of the laser amplitude and is accompanied by a strong electrostatic field $E_x(x,t)$. Figure 4(d) shows that the power of the backscattered wave has increased by about an order of magnitude compared to that in Fig. 4(c). This increase is caused by the larger amplitude and the wider spatial interval, in which the secondary waves grow. At the end of the time interval covered by box 3, the secondary waves grow in the entire interval that is filled with electrons.

The time scale of the interaction and the amplitudes of the secondary waves in Figs. 4(a) and 4(e) are, in general, comparable to those in the Vlasov simulations in Figs. 2(a)–2(f), even though details in the time evolution differ somewhat due to the statistical nature of the numerical noise in the PIC simulation and of the external random noise introduced in the Vlasov simulations. In both the Vlasov and PIC simulations, the secondary waves are visible after the $\omega_0 t \sim 7000 - 10\,000$. The back-scattered light in the Vlasov and PIC simulations in Figs. 2(a), 2(c), and 2(e), and 4(a) have normalized amplitudes of $\sim 2 \times 10^{-3}$ in the initial bursts and later reach larger amplitudes of $\sim 6 - 9 \times 10^{-3}$. The electrostatic waves also in both simulations shown in Figs. 2(b), 2(d), 2(f), and 4(e) reach normalized amplitudes of $\sim 1 - 2 \times 10^{-3}$ with the slightly higher peak amplitudes reached in the Vlasov simulations.

Figure 5 examines in more detail the properties of the electrostatic waves in the distribution of $E_x(x,t)$ and of the corresponding phase space density distributions of electrons. Fourier spectra are computed over the same spatiotemporal intervals as in Fig. 4 while the electron distributions are sampled at the central times of each box.

Figures 5(a) and 5(e) show the electrostatic wave spectrum and the associated electron distribution in box 1. The noise spectrum peaks at the Langmuir wave branch and broadband noise is present in intervals where ω/k is below a few times v_{Te}. The noise power at $\omega = 1.5\,\omega_{pe}$ rises for $k\lambda_{De} > 0.3$, which corresponds to phase speeds below $5\,v_{Te}$. At this time, the power near the secondary Langmuir wave is at noise levels comparable to the theoretical thermal noise spectrum in Fig. 1. The electron distribution is spatially uniform at this time. Any amplitudes of Raman scattering at this time of the secondary waves are close to noise levels.

Figure 5(b) shows the Fourier spectrum of the electric field in box 2 of Fig. 4(e), when strong electrostatic waves fills up half of the box. Here, the Fourier spectrum contains wave contributions both from the Maxwell-distributed electrons in thermal equilibrium, and from the non-thermal electrons and collective fluctuations in the heated plasma. Strong waves are located near the wavenumber k_L and frequency ω_L of the secondary Langmuir wave, indicated by a ring in Fig. 5(b). The power peaks at k_L and at a frequency just below ω_L. The noise power in the quadrant $k < 0$ is not affected at this time; electrons with $v_x < 0$ have kept their thermal distribution. Figure 5(f) reveals the presence of electron phase space holes around the phase velocity $v_{ph,L}/v_{Te} = 3.5$

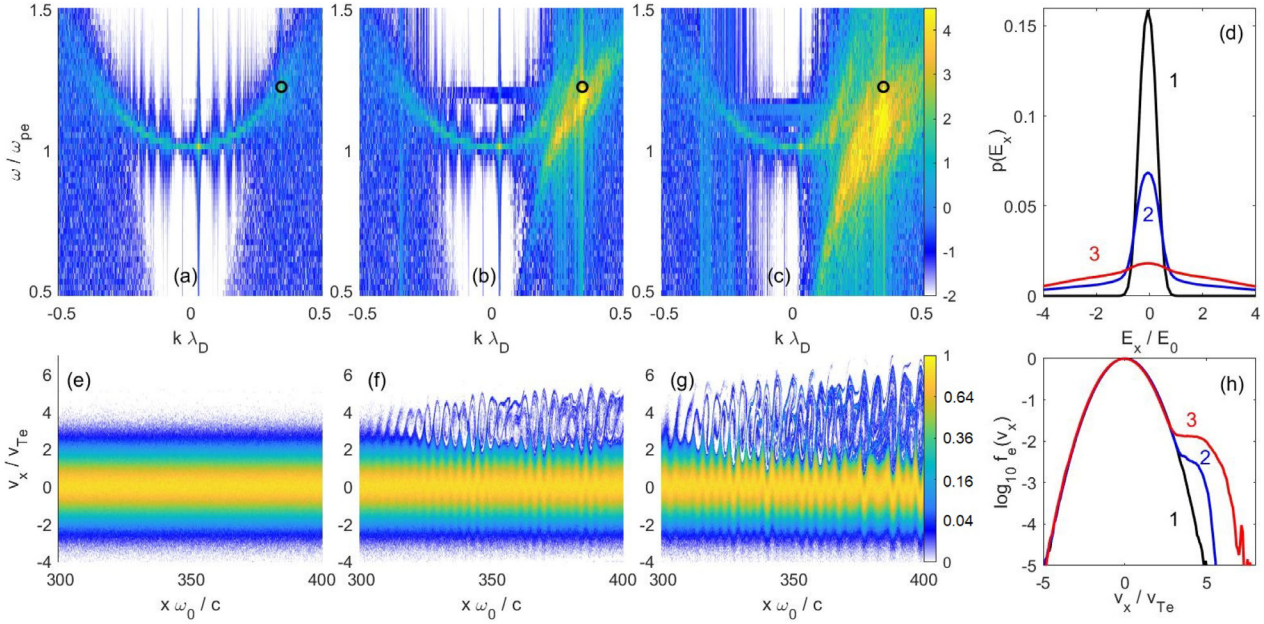

FIG. 5. PIC simulation showing the properties and consequences of the Langmuir wave: Panels (a)–(c) show the power spectra of $E_x(x,t)$ in the boxes (1–3) in Fig. 4. The circles mark $(\omega,k)=(\omega_L,k_L)$. Panel (d) plots the probability distributions of the electric field amplitudes $E_x(x,t)$ in units of E_{rand} with $eE_{rand}/\omega_0 m_e c = 1.25\times10^{-4}$. in boxes 1–3. Panels (e)–(g) show the electron phase space densities in the subinterval $300 \le x\,\omega_0/c \le 400$ at the central times in boxes 1–3 (observe that the color scale enhances low values of f_e for improved visibility.). Panel (h) shows the electron velocity distributions v_x at the central times of boxes 1–3, which have been integrated over the entire box. All distributions were normalized to the peak value of the black curve and plotted on a 10-logarithmic scale. The black curves in (d) and (h) correspond to interval 1, the blue ones to interval 2, and the red curves to interval 3. See the movie showing the dynamics of the system in the supplementary material.

of the resonant Langmuir wave (cf. Table I). The phase space density of electrons with $v_x > 4v_{Te}$ is well above that in box 1 and their large electric current induces the strong wave components seen in the Fourier spectrum. The phase space holes are not periodic anymore; they have started to undergo coalescence instability,[73–75] as also seen in the Vlasov simulation in Fig. 3. As the phase space holes merge and increase in size, their mean velocities change, explaining the cascade of wave power across wide intervals of lower wavenumbers and frequencies seen as oblique yellow streaks in Figs. 5(b) and 5(c). These low-frequency waves rest on the slow electron-acoustic branch which is heavily damped in linear Vlasov theory but can be weakly damped nonlinearly and if the distribution function develops a plateau.[72] Signatures of the trapped-electron acoustic mode was also seen in the experiment by Montgomery *et al.*[27] where scattering from a plasma wave with frequency between the ion-acoustic and plasma frequency was observed. The electron phase space holes have a mean speed that exceeds v_{Te} by a factor 3, and they, thus, propagate to larger x carrying the trapped electrons with them. The lost electrons are replaced by those of the thermal plasma with $v_x < 0$, which get wrapped around at the left boundary of the plasma at $x\omega_0/c \approx 300$ and move to larger x. Their inflow brings the electrons in the interval with $v_x > 0$ closer to their initial thermal equilibrium, thus paving the way for a new burst. The largest burst in box 3 has created a chain of aperiodic electron phase space holes in Fig. 5(g). The peak electron velocity has now increased to about $6.5v_{Te}$. Their wave spectrum has broadened and intensified in Fig. 5(c). The evolution of the electron phase space density in the interval $300 \le x\omega_0/c \le 400$ and of the amplitudes of both secondary waves is visualized in the supplementary movie. It shows clearly the correlation between the onset of SRBS and the formation of electron phase space holes.

Figures 5(d) and 5(h) show the probability distributions $p(E_x)$ of the electric field $E_x(x,t)/E_{rand}$ computed in the three boxes and the electron velocity distributions in each box integrated over x. Here, E_{rand} is the external noise electric field for $eE_{rand}/\omega_0 m_e c = 1.25\times10^{-4}$. The electron velocity distribution in box 1 is Maxwellian and the noise spectrum should be close to that of thermal noise. Indeed, the noise amplitudes in box 1 are comparable to our estimate E_{rand} of the peak noise amplitude that is based on the fluctuation–dissipation theorem in thermal electron plasma. The distribution is, however, closer to a Gaussian distribution than to the externally imposed rectangular distribution in the Vlasov simulations. The electric field distributions in boxes 2 and 3 show that the typical electric field amplitudes are much larger than E_{rand}. The value of $p(E_x)$ still shows a dominant peak in the interval $-E_{rand} \le E_x \le E_{rand}$ in box 2 and has the same width as the one in box 1. We attribute this peak to the electric fields in the spatial interval $x\omega_0/c > 900$ with no enhanced wave activity in Figs. 4(a) and 4(e). A hump in the electron velocity distribution is growing for velocities above $\omega_L/k_L \approx 3.5v_{Te}$ in the curve for box 2. This hump has developed into a plateau in box 3, which reduces the Landau damping and enhances the SRBS process.

C. Vlasov simulations with injected seed waves

Wang *et al.*[35] carried out Vlasov simulations with a seed laser injected from the opposite boundary of the pump to seed the SRBS instability, and could explain the experimental results of Montgomery

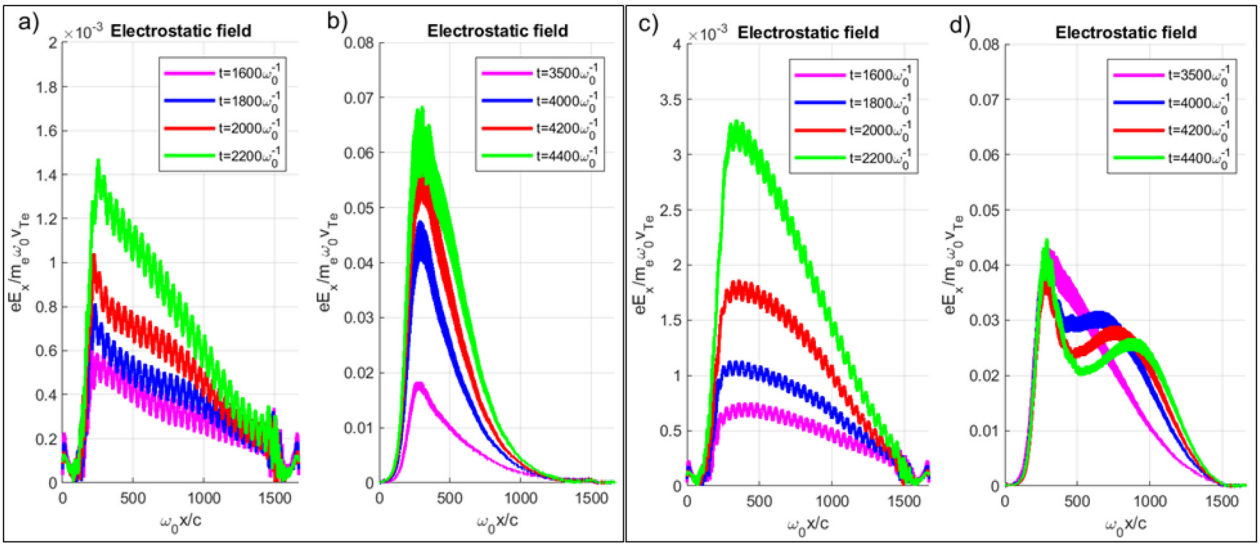

FIG. 6. The electrostatic wave field as a function of space at different times obtained in Vlasov simulations, for $a_0 = 0.0246$, seed amplitude $10^{-3}a_0$, and the frequency downshift of the seed equal to (a) and (b) $\omega_L = 1.178\omega_{pe}$ and (c) and (d) $\omega_L = 1.2233\omega_{pe}$.

et al.,[27] even though a seed pulse was not used in the experiment. We here carry out a set of Vlasov simulations with a seed wave but without random noise. The purpose is to reproduce and confirm the numerical result of Wang *et al.*[35] using a different simulation code, and to investigate the sensitivity of the results on the laser parameters.

To drive the electron plasma wave resonantly, we use a frequency downshifted seed where the beat frequency equals that of the electron plasma wave.[76] First, a laser pump wave of intensity $I_0 = 3.0 \times 10^{15}\mathrm{W/cm^2}$ (cf. Table II) is injected at the left boundary and a low-amplitude counter-propagating seed wave of $10^{-6}\, I_0$ at the right boundary, having a slightly lower frequency compared to the pump in order to resonantly drive a Langmuir wave. Estimating the resonant Langmuir wavenumber to be $k_L = 0.35\,\lambda_{De}^{-1}$[35] and tuning the frequency of the seed pulse to $\omega_1 = \omega_0 - \omega_L$ with $\omega_L = 1.178\,\omega_{pe}$, roughly consistent with the Bohm-Gross dispersion relation $\omega_L^2 = \omega_{pe}^2 + 3v_{Te}^2k_L^2$, the results in Figs. 6(a) and 6(b) reproduce the ones by Wang *et al.*[35] in their Fig. 2. However, for $\lambda_{De}^2k_L^2 > 0.25$ the Bohm–Gross approximation becomes inaccurate.[27,77] More exact linear Vlasov theory gives $k_L = 0.3518\,\lambda_{De}^{-1}$ and $\omega_L = 1.2233\,\omega_{pe}$ for the resonant 3-wave interaction, with a linear Landau damping rate $\gamma_L = 0.0353\,\omega_{pe}$. It is seen in Fig. 6(c) that this gives a faster growth resulting in a few times higher amplitudes of the backscattered signal compared to Fig. 6(a). The faster time development also leads to that the instability has reached nonlinear saturation in Fig. 6(d) while the amplitude is still growing with time in Fig. 6(b).

To analyze the detailed structure of the instability in Figs. 6(c) and 6(d), the spatiotemporal evolutions of the backscattered light and electrostatic fluctuations are plotted in Fig. 7. The convective instability initially grows slowly in space and reaches its low amplitude maximum at the left boundary, as seen at $\omega_0 t \approx 3.0 \times 10^3$ in Fig. 7(a). The spatial amplification grows with time and reaches saturation near the left boundary at $\omega_0 t \approx 3.5 \times 10^3$; this is a signature that the electron distribution function evolves in time and develops a plateau and phase space holes near the phase velocity $v_{ph,L} = \omega_L/k_L$ of the resonant Langmuir wave, as illustrated in Figs. 3 and 5 above. After this, the saturation layer shifts toward the right as the convective amplification increases further. At $\omega_0 t \approx 7 \times 10^3$ to 11×10^3, an inflationary growth of the instability as described by Wang *et al.*[35] takes place, in which large amplitude pulses of backscattered light are excited by rapid growth in time in the spatial region $\omega_0 x/c = 600 - 800$ [cf. Fig. 7(a)]. The beating between the pump laser and large amplitude backscattered pulses of light results in large amplitude nonlinear Langmuir waves

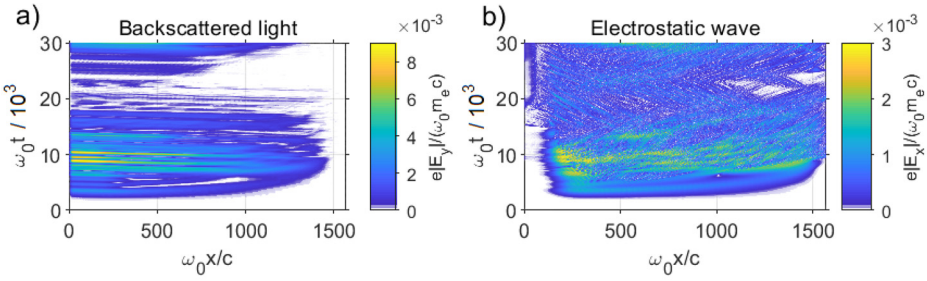

FIG. 7. Vlasov simulation showing the normalized amplitude of (a) the backscattered EM wave E_y and (b) the electrostatic wave E_x and for $a_0 = 0.0246$, seed amplitude $10^{-3}a_0$, and $\omega_L = 1.2233\,\omega_{pe}$.

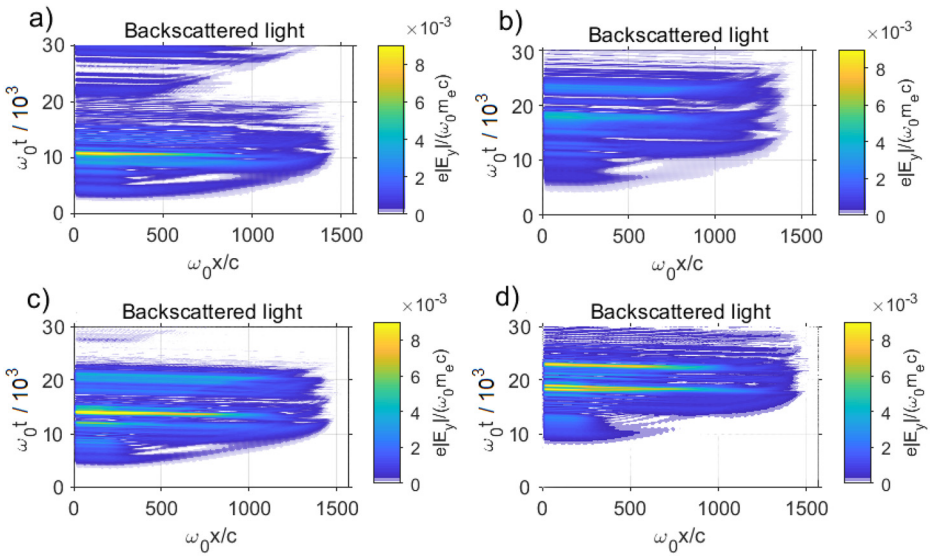

FIG. 8. Vlasov simulations showing the normalized amplitude of the back-scattered laser for normalized laser amplitude (a) $a_0 = 0.02$ and (b) $a_0 = 0.015$, and the respective seed amplitude $10^{-3}a_0$. In panels (c) and (d), the seed amplitude is decreased to $10^{-4}a_0$ and $10^{-5}a_0$, respectively, for $a_0 = 0.0246$. The frequency down-shift of the seed pulse relative to the pump is $\omega_L = 1.2233\,\omega_{pe}$ for all cases.

and a decrease in the backscattered light at later times due to the detuning of the resonant Raman interaction.

Figure 8 shows the spatiotemporal evolution of the backscattered light for lower amplitudes of the injected laser and seed wave: In panels (a) and (b), the normalized laser amplitude is $a_0 = 0.02$ and 0.015, respectively, for the seed amplitude $10^{-3}a_0$, and in panels (c) and (d), the seed amplitude is decreased to $10^{-4}a_0$ and $10^{-5}a_0$, respectively, for $a_0 = 0.0246$. Compared to Fig. 7(a), the evolution is qualitatively similar as in Fig. 8. For lower injected laser amplitudes [Figs. 8(a) and 8(b)], the nonlinear evolution is delayed in time and the backscattered light is of lower amplitude, and for lower seed amplitudes [Figs. 8(c) and 8(d)], keeping the pump unchanged the nonlinear evolution is delayed in time but the backscattered light reaches the same amplitude as in Fig. 7(a). However, decreasing the injected seed amplitude to zero (not shown) the SRBS instability does not develop within the simulation time.

VI. CONCLUSIONS

The present work has shown the importance of thermal noise in stimulated Raman backscattering (SRBS) instability in the regime where the resonant Langmuir wave is initially heavily Landau damped, and the SRBS instability is in the regime of convective growth of weak thermal emissions in the plasma. Vlasov and particle-in-cell (PIC) simulations are employed to study the inflation phenomenon and are configured to mimic the thermal emissions on a level predicted for the given plasma parameters. As the resonantly driven electron plasma oscillations are linearly Landau damped, the electron distribution function gradually develops a plateau in velocity space close to the resonant velocity equal to the phase velocity of the Langmuir wave. This leads to a decrease in the Landau damping with time and an increase in the convective amplification of the scattered waves. When the Langmuir wave reaches a high enough amplitude, it starts trapping electrons in the wave potential, leading to further decrease in the Landau damping and a rapid absolute instability that was studied earlier by Wang *et al.*[35] This results in transient spikes of large amplitude reflected light[29] and rapid acceleration of electrons forming high-energy tails in the distribution function.

In the numerical simulations, the spatial resolution should be high enough to capture the electrostatic wave, which has the shortest wavelength of the three waves. According Table I and consistent with Figs. 3 and 5, the resonant Langmuir wave has the wavenumber $k_L = 0.35\lambda_{De}^{-1} = 21.2 \times 10^6\ \mathrm{m}^{-1}$, which is well below the Nyquist wavenumber $k_{Nyquit} = \pi/\Delta x = 45 \times 10^7\ \mathrm{m}^{-1}$ in the simulations, and the Langmuir wave is resolved by about 42 grid points per wavelength, which is large enough to resolve the wave accurately itself and trapped particles/phase space holes in the wave. To get a quantitatively correct representation of thermal noise in PIC simulations, we also need as many computational particles per Debye length as in a real plasma, which we have estimated to be of the order $N_{De} = (2\pi)^2\lambda_{De}^3 n_e = 18\,000$ for the laser-plasma parameters considered here. Electron–ion collisions are relatively unimportant due to the low density of the plasma. However, mild numerical dissipation is needed in the Vlasov simulations to avoid aliasing effect in space and recurrence effects in momentum space, as discussed in Sec. II.

Our model is idealized in that it assumes a spatially uniform electron plasma and is limited to one spatial dimension, which excludes effects such as side scattering, beam filamentation, and higher-dimensional effects on numerical noise. Resolving two spatial dimensions would facilitate instabilities of the electron phase space tubes that result in their spatial variation along the tube axis. Once they stop being planar, the backscattering might get weaker, and one may get patches of backscattering when the phase space holes do not grow uniformly in the perpendicular plane. Also, since the Langmuir waves grow out of random noise, they will not be planar. Future work, thus, should assess how a nonuniform distribution of the electrostatic waves in oblique directions to the laser beam direction affects the instability. In addition, the limited diameter of the laser beam will introduce a potentially important nonuniformity of the plasma. Parametric studies are also needed to determine how strongly the growth of the secondary waves depends on the noise levels and details of the electron velocity distribution, as well as a variation of the laser-to-plasma frequency

ratio up to the quarter-critical density where absolute Raman scattering instability is prominent.[18,19] For the Vlasov simulations, a more precise way to introduce external fluctuations consistent with thermal noise should be considered.

Finally, it should be noted that PIC simulations have the advantage over Vlasov simulations in that that they introduce thermal noise-like fluctuations self-consistently, via a numerical version of the fluctuation–dissipation theorem.[46–48] However, in dilute and warm plasma where the plasma parameter $\lambda_{De}^3 n_e$ can become very large, the high number of computational particles required in PIC simulations to model real thermal noise can be unfeasible, and for this case, Vlasov simulations with carefully introduced external noise may be used to model the interaction. In this regard, laser-plasma parameters with moderately large plasma parameters constitute an ideal test-bed to compare both methods with each other and with experiment.

SUPPLEMENTARY MATERIAL

See the supplementary material for time evolution of the electron distribution function in the Vlasov simulation in Figs. 2(a) and 2(b) and Fig. 3 is shown in one movie for the region $2-4\times10^{-5}$ m near the left plasma boundary and one movie for the whole space domain $0-1.4\times10^{-4}$ m. The results of the PIC simulation are shown in a movie containing the time evolutions of the electric fields E_x and E_y and the electron distribution function, which are discussed in Figs. 4 and 5.

ACKNOWLEDGMENTS

Vlasov simulation results were obtained using the ARCHIE-WeSt High Performance Computer (https://www.archie-west.ac.uk) based at the University of Strathclyde. The PIC computations/data handling was enabled by resources provided by the National Academic Infrastructure for Supercomputing in Sweden (NAISS) at the National Supercomputer Centre partially funded by the Swedish Research Council through Grant Agreement No. 2022-06725. B.E. acknowledges support from the EPSRC (UK), Grant Nos. EP/R004773/1 and EP/M009386/1. X.Y.J. and Z.M.S. acknowledge support by the Strategic Priority Research Program of Chinese Academy of Sciences (Grant No. XDA25050100) and the National Natural Science Foundation of China (Grant Nos. 11991074 and 12135009). This work has been carried out within the framework of the EUROfusion Consortium, funded by the European Union via the Euratom Research and Training Programme (Grant Agreement No. 101052200-EUROfusion). Views and opinions expressed are however those of the authors only and do not necessarily reflect those of the European Union or the European Commission.

AUTHOR DECLARATIONS

Conflict of Interest

The authors have no conflicts to disclose.

Author Contributions

B. Eliasson: Software (equal); Writing – original draft (equal); Writing – review & editing (equal). **M. E. Dieckmann:** Investigation (equal); Writing – review & editing (equal). **X. Jiang:** Investigation (supporting). **Z. M. Sheng:** Investigation (supporting). **C. S. Liu:** Conceptualization (equal).

DATA AVAILABILITY

The data that support the findings of this study are available within the article and its supplementary material.

APPENDIX: DRESSED PARTICLE APPROACH, 1D

For application to 1D PIC and Vlasov simulations, we derive the thermal noise spectrum for a 1D geometry in space, using the test particle approach as previously described by Krall and Trivelpiece[40] for the 3D case. In a 1D geometry with variations only along the x-axis, say, the test particle is a point-particle in the x-direction, but extends indefinitely in the y- and z-directions, essentially forming a moving infinitely wide plate. Although we first assume that the particles are described by delta-functions, we show at the end of the calculations below that it is straightforward to take into account particles described by finite-width shape functions such as those used in PIC simulations. In our electrostatic case, we assume that the test particle moves only in the x-direction. A test particle having charge density ρ^{2D} (in C/m^2) in the y-z plane and moving with velocity v_0 gives the charge density

$$\rho_{\rm test}(x,t)=\rho^{2D}\delta(x-x_0-v_0t). \tag{A1}$$

Introducing the spatiotemporal Fourier transform pair

$$\hat\rho(k,\omega)=\int\int\rho(x,t)e^{-ikx+i\omega t}\,dx\,dt, \tag{A2}$$

$$\rho(x,t)=\frac{1}{(2\pi)^2}\int\int\hat\rho(k,\omega)e^{ikx-i\omega t}\,dk\,d\omega \tag{A3}$$

and Fourier transforming the test charge density (A1) over space and time gives

$$\hat\rho_{\rm test}(k,\omega)=2\pi\rho^{2D}\delta(\omega-kv_0)e^{-ikx_0}, \tag{A4}$$

where δ is Dirac's delta function. The self-consistent electrostatic potential is obtained from Poisson's equation,

$$\frac{\partial^2}{\partial x^2}\phi(x,t)=-\frac{1}{\epsilon_0}(\rho_{\rm plasma}(x,t)+\rho_{\rm test}(x,t)). \tag{A5}$$

Fourier transformation gives

$$-k^2\hat\phi(k,\omega)=-\frac{1}{\epsilon_0}(\hat\rho_{\rm plasma}(k,\omega)+\hat\rho_{\rm test}(k,\omega)) \tag{A6}$$

or

$$\hat\phi(k,\omega)=\frac{1}{\epsilon_0k^2}(\hat\rho_{\rm plasma}(k,\omega)+2\pi\rho^{2D}\delta(\omega-kv_0)e^{-ikx_0}). \tag{A7}$$

The plasma response is found by solving the linearized evolution equation for the plasma, giving the linear relation between $\hat\rho_{\rm plasma}(k,\omega)$ and $\hat\phi(k,\omega)$,

$$\hat\rho_{\rm plasma}(k,\omega)=-\epsilon_0k^2\chi_{\rm L}(k,\omega)\hat\phi(k,\omega), \tag{A8}$$

where $\chi_{\rm L}(k,\omega)$ is the susceptibility for longitudinal waves. Denoting the dielectric constant $\varepsilon_{\rm L}(k,\omega)=1+\chi_{\rm L}(k,\omega)$ gives

$$\hat\phi(k,\omega)=\frac{2\pi\rho^{2D}e^{-ikx_0}}{\epsilon_0\varepsilon_{\rm L}(k,\omega)k^2}\delta(\omega-kv_0). \tag{A9}$$

Taking the inverse Fourier transform gives the potential

$$\phi(x,t) = \frac{1}{(2\pi)^2}\int\int \hat{\phi}(k,\omega)e^{ikx-i\omega t}dk\,d\omega = \int \frac{\rho^{2D}e^{ik(x-\tilde{x}_0(t))}}{\epsilon_0\varepsilon_L(k,kv_0)k^2}\frac{dk}{2\pi}, \tag{A10}$$

where $\tilde{x}_0(t) = x_0 + v_0 t$, and the electric field

$$E(x,t) = -\frac{\partial\phi}{\partial x} = -\int \frac{\rho^{2D}ike^{ik(x-\tilde{x}_0(t))}}{\epsilon_0\varepsilon_L(k,kv_0)k^2}\frac{dk}{2\pi}. \tag{A11}$$

The squared electric field averaged over x_0 and v_0 is obtained as

$$\begin{aligned}\langle E^2\rangle &= \int\int n_e^{1D}EE^*dx_0 f_{e0}^{1D}(v_0)dv_0 \\ &= \frac{(\rho^{2D})^2 n_e^{1D}}{\epsilon_0^2}\int\int\int \frac{ike^{ik(x-\tilde{x}_0)}}{\varepsilon_L(k,kv_0)k^2}\frac{dk}{2\pi} \\ &\quad\times\int \frac{-ik'e^{-ik'(x-\tilde{x}_0)}}{\varepsilon_L^*(k',k'v_0)(k')^2}\frac{dk'}{2\pi}d\tilde{x}_0 f_{e0}^{1D}(v_0)dv_0,\end{aligned} \tag{A12}$$

where n_e^{1D} is the number of test electrons per unit length, and the asterisk denotes complex conjugation. The electron distribution function is normalized such that $\int f_{e0}^{1D}(v_0)\,dv_0 = 1$. The integration over $\tilde{x}_0$ gives rise to an integral of the form

$$\int e^{i(k'-k)x_0}\,dx_0 = 2\pi\delta(k'-k), \tag{A13}$$

with the result that

$$\langle E^2\rangle = \frac{(\rho^{2D})^2 n_e^{1D}}{\epsilon_0^2}\int\int\int \frac{2\pi\delta(k'-k)e^{i(k-k')x}f_{e0}^{1D}(v_0)}{\varepsilon_L(k,kv_0)\varepsilon_L^*(k',k'v_0)kk'}\times\frac{dk'}{2\pi}\frac{dk}{2\pi}\,dv_0. \tag{A14}$$

Carrying out the integral with respect to k' gives

$$\langle E^2\rangle = \frac{(\rho^{2D})^2 n_e^{1D}}{\epsilon_0^2}\int\int \frac{f_{e0}^{1D}(v_0)}{|\varepsilon_L(k,kv_0)|^2k^2}\frac{dk}{2\pi}\,dv_0. \tag{A15}$$

By the change of integration variable $v_0 = \omega/k$, one obtains

$$\int \frac{f_{e0}^{1D}(v_0)}{|\varepsilon_L(k,kv_0)|^2k^2}\,dv_0 = \int \frac{f_{e0}^{1D}(\omega/k)}{|\varepsilon_L(k,\omega)|^2k^3}\,d\omega. \tag{A16}$$

The special case of a 1D Maxwellian electron distribution function,

$$f_{e0}^{1D}(v_x) = \frac{1}{(2\pi)^{1/2}v_{Te}}\exp\left(-\frac{v_x^2}{2v_{Te}^2}\right), \tag{A17}$$

gives

$$f_{e0}^{1D}(\omega/k) = \frac{e^{-\xi_e^2}}{(2\pi)^{1/2}v_{Te}}, \tag{A18}$$

where $\xi_e = \omega/\left(\sqrt{2}|k|v_{Te}\right)$. The electron dielectric function is

$$\varepsilon_L = 1 + \frac{\omega_{pe}^2}{k^2v_{Te}^2}[1 + \xi_e Z(\xi_e)], \tag{A19}$$

where $Z(\xi) = i\sqrt{\pi}e^{-\xi^2} - 2w_D(\xi)$ is the plasma dispersion function[66] with

$$w_D(\xi) = e^{-\xi^2}\int_0^\xi e^{t^2}\,dt \tag{A20}$$

being Dawson's integral.[67] We then can express

$$\int \frac{f_{e0}^{1D}(\omega/k)}{|\varepsilon_L(k,\omega)|^2k^3}d\omega = \int \frac{e^{-\xi_e^2}}{(2\pi)^{1/2}v_{Te}|\varepsilon_L(k,\omega)|^2k^3}d\omega. \tag{A21}$$

Noting from Eq. (A19) that

$$e^{-\xi^2} = \frac{k^2v_{Te}^2}{\omega_{pe}^2\xi_e\sqrt{\pi}}\Im(\varepsilon_L) = \frac{k^3v_{Te}^3\sqrt{2}}{\omega_{pe}^2\omega\sqrt{\pi}}\Im(\varepsilon_L), \tag{A22}$$

one has

$$\int \frac{f_{e0}^{1D}(\omega/k)}{|\varepsilon_L(k,\omega)|^2k^3}d\omega = \int \frac{v_{Te}^2\Im(\varepsilon_L)}{\pi\omega_{pe}^2\omega|\varepsilon_L(k,\omega)|^2}d\omega \tag{A23}$$

and

$$\begin{aligned}\langle E^2\rangle &= \frac{(\rho^{2D})^2 n_e^{1D}}{\epsilon_0^2}\int\int \frac{v_{Te}^2\Im(\varepsilon_L)}{\pi\omega_{pe}^2\omega|\varepsilon_L|^2}\frac{dk}{2\pi}\,d\omega \\ &= -\frac{2k_BT_e}{\epsilon_0}\frac{(\rho^{2D})^2 n_e^{1D}}{\epsilon_0 m_e\omega_{pe}^2}\int\int \frac{1}{\omega}\Im\left(\frac{1}{\varepsilon_L}\right)\frac{dk}{2\pi}\frac{d\omega}{2\pi}.\end{aligned} \tag{A24}$$

The spectral density is finally obtained as the integrand of Eq. (A24), as

$$W^{1D}(k,\omega) = -\frac{2}{(2\pi)^2}\frac{k_BT_e}{\omega\epsilon_0}\frac{(\rho^{2D})^2 n_e^{1D}}{\epsilon_0 m_e\omega_{pe}^2}\Im\left(\frac{1}{\varepsilon_L}\right). \tag{A25}$$

We briefly discuss the effect of finite width computational particles in PIC simulations on the noise spectrum. We can understand the effects of the particle shape (or support) function by realizing that a computational particle (CP) is a point particle convolved with the shape function of the CP. This amounts to replacing the δ-function in Eq. (A1) by the shape function $S(\xi)$ so that the test charge takes the form

$$\rho_{test}(x,t) = \rho^{2D}S(x - x_0 - v_0 t). \tag{A26}$$

This leads to a Fourier transformed potential of the form

$$\hat{\phi}(k,\omega) = \frac{2\pi\rho^{2D}e^{-ikx_0}}{\epsilon_0\varepsilon_L(k,\omega)k^2}\hat{S}(k)\delta(\omega - kv_0), \tag{A27}$$

which differs from Eq. (A9) only by the extra factor $\hat{S}(k)$, being the Fourier transformed shape function. The multiplication by $\hat{S}(k)$ carries through the rest of the calculations leading to the spectral density

$$W^{1D}(k,\omega) = -\frac{2}{(2\pi)^2}\frac{k_BT_e}{\omega\epsilon_0}\frac{(\rho^{2D})^2 n_e^{1D}}{\epsilon_0 m_e\omega_{pe}^2}|\hat{S}(k)|^2\Im\left(\frac{1}{\varepsilon_L}\right), \tag{A28}$$

which has the extra factor $|\hat{S}(k)|^2$ compared to Eq. (A25). For small values of k, the Fourier transformed shape function $\hat{S}(k) \approx 1$ and one recovers Eq. (A25), and the numerical noise resembles thermal noise, as was found numerically by Dieckmann *et al.*[48] In Epoch, the lowest order shape function is the discontinuous "top-hat" function of width Δx with a Fourier transformed shape function of the

form $\hat{S}_{th}(k) = \sin(kD)/(kD)$ with $D = \Delta x/2$ being the half-width of the shape function. The triangular shape function used in the present PIC simulations, which is continuous but twice as wide in space, is obtained by a convolution of the top-hat shape function by itself, which in the Fourier transformed space leads multiplication by itself due to the convolution theorem, $\hat{S}_{tri}(k) = \hat{S}_{th}(k)^2 = [\sin(kD)/(kD)]^2$. This procedure may be continued to higher orders (and wider in space) shape functions with continuous derivatives of increasing orders. Changing the shape function mostly affects the noise power at the highest resolved wavenumbers, where higher order shape functions reduces the noise power and avoids detrimental aliasing effects across the Nyquist wavenumber $\pi/\Delta x$. Detailed discussion about shape functions as well as the effect of grid boundaries in space and time on numerical noise in PIC simulations can be found in Chap. 12 of Ref. 46 as well as in Refs. 47 and 56.

REFERENCES

[1]R. K. Kirkwood, J. D. Moody, J. Kline, E. Dewald, S. Glenzer, L. Divol, P. Michel, D. Hinkel, R. Berger, and E. Williams, "A review of laser–plasma interaction physics of indirect–drive fusion," Plasma Phys. Controlled Fusion **55**, 103001 (2013).

[2]D. S. Montgomery, "Two decades of progress in understanding and control of laser plasma instabilities in indirect drive inertial fusion," Phys. Plasmas **23**, 055601 (2016).

[3]R. Bingham, J. T. Mendonça, and P. K. Shukla, "Plasma based charged-particle accelerators," Plasma Phys. Controlled Fusion **46**, R1 (2004).

[4]J. P. Farmer, B. Ersfeld, and D. A. Jaroszynski, "Raman amplification in plasma: Wavebreaking and heating effects," Phys. Plasmas **17**, 113301 (2010).

[5]R. M. G. M. Trines, E. P. Alves, E. Webb, J. Vieira, F. Fiùza, R. A. Fonseca, L. O. Silva, R. A. Cairns, and R. Bingham, "New criteria for efficient Raman and Brillouin amplification of laser beams in plasma," Sci. Rep. **10**, 19875 (2020).

[6]G. Vieux, S. Cipiccia, G. H. Welsh, S. R. Yoffe, F. Gärtner, M. P. Tooley, B. Ersfeld, E. Brunetti, B. Eliasson, C. Picken, G. McKendrick, M.-S. Hur, J. M. Dias, T. Kühl, G. Lehmann, and D. A. Jaroszynski, "The role of transient plasma photonic structures in plasma-based amplifiers," Commun. Phys. **6**, 9 (2023).

[7]C. S. Liu, M. N. Rosenbluth, and R. B. White, "Raman and Brillouin scattering of electromagnetic waves in inhomogeneous plasmas," Phys. Fluids **17**, 1211 (1974).

[8]J. F. Drake, P. K. Kaw, Y. C. Lee, G. Schmid, C. S. Liu, and M. N. Rosenbluth, "Parametric instabilities of electromagnetic waves in plasmas," Phys. Fluids **17**, 778 (1974).

[9]C. S. Liu, V. K. Tripathi, and B. Eliasson, *High-Power Laser-Plasma Interaction* (Cambridge University Press, 2019), Chap. 10.

[10]W. L. Kruer, *The Physics of Laser Plasma Interactions*, 1st ed. (CRC Press, 2003).

[11]Z.-M. Sheng, K. Nishihara, T. Honda, Y. Sentoku, K. Mima, and S. V. Bulanov, "Anisotropic filamentation instability of intense laser beams in plasmas near the critical density," Phys. Rev. E **64**, 066409 (2001).

[12]W. Kruer, S. Wilks, B. Afeyan, and R. Kirkwood, "Energy transfer between crossing laser beams," Phys. Plasmas **3**, 382–385 (1996).

[13]P. Michel, L. Divol, E. Williams, C. Thomas, D. Callahan, S. Weber, S. Haan, J. Salmonson, N. Meezan, O. Landen, and S. Dixit, "Energy transfer between laser beams crossing in ignition *Hohlraums*," Phys. Plasmas **16**, 042702 (2009).

[14]H. Schmitz, R. Trines, and R. Bingham, "Transverse beam envelope structures in strongly coupled stimulated Brillouin scattering," Phys. Plasmas **27**, 102707 (2020).

[15]X. T. He, J. W. Li, Z. F. Fan, L. F. Wang, J. Liu, K. Lan, J. F. Wu, and W. H. Ye, "A hybrid-drive nonisobaric-ignition scheme for inertial confinement fusion," Phys. Plasmas **23**, 082706 (2016).

[16]K. Lan, K. J. Liu, Z. Li, X. Xie, W. Huo, Y. Chen, G. Ren, C. Zheng, D. Yang, S. Li, Z. Yang, L. Guo, S. Li, M. Zhang, X. Han, C. Zhai, L. Hou, Y. Li, K. Deng, Z. Yuan, X. Zhan, F. Wang, G. Yuan, H. Zhang, B. Jiang, L. Huang, W. Zhang, K. Du, R. Zhao, P. Li, W. Wang, J. Su, X. Deng, D. Hu, W. Zhou, H. Jia, Y. Ding, W. Zheng, and X. He, "Progress in octahedral spherical *Hohlraum* study," Matter Radiat. Extremes **1**, 8 (2016).

[17]W. Huo, Z. Li, D. Yang, K. Lan, J. Liu, G. Ren, S. Li, Z. Yang, L. Guo, L. Hou, X. Xie, Y. Li, K. Deng, Z. Yuan, X. Zhan, G. Yuan, H. Zhang, B. Jiang, L. Huang, K. Du, R. Zhao, P. Li, W. Wang, J. Su, Y. Ding, X. He, and W. Zhang, "First demonstration of improving laser propagation inside the spherical *Hohlraums* by using the cylindrical laser entrance hole," Matter Radiat. Extremes **1**, 2 (2016).

[18]M. J. Rosenberg, A. A. Solodov, J. F. Myatt, W. Seka, P. Michel, M. Hohenberger, R. W. Short *et al.*, "Origins and scaling of hot-electron preheat in ignition-scale direct-drive inertial confinement fusion experiments," Phys. Rev. Lett. **120**(5), 055001 (2018).

[19]R. White, P. Kaw, D. Pesme, M. N. Rosenbluth, G. Laval, R. Huff, and R. Varma, "Absolute parametric instabilities in inhomogeneous plasmas," Nucl. Fusion **14**, 45–51 (1974).

[20]M. Luo, S. Hüller, M. Chen, and Z. M. Sheng, "On the role of bandwidth in pump and seed light waves for stimulated Raman scattering in inhomogeneous plasmas," Phys. Plasmas **29**(3), 032102 (2022).

[21]Y. Zhao, S. M. Weng, H. H. Ma, X.-J. Bai, and Z.-M. Sheng, "Mitigation of laser plasma parametric instabilities with broadband lasers," Rev. Mod. Plasma Phys. **7**(1), 1 (2023).

[22]X. Y. Jiang, S. M. Weng, H. H. Ma, X. F. Li, C. F. Wu, Z. Liu, Y. Zhao, M. Chen, and Z. M. Sheng, "Broadband electromagnetic emission via mode conversion mediated by stimulated Raman scattering in inhomogeneous plasma," Phys. Plasmas **30**(2), 022105 (2023).

[23]H. Abu-Shawareb, R. Acree, P. Adams, J. Adams, B. Addis, R. Aden, P. Adrian, B. B. Afeyan, M. Aggleton, L. Aghaian *et al.*, "Lawson criterion for ignition exceeded in an inertial fusion experiment," Phys. Rev. Lett. **129**, 075001 (2022).

[24]A. L. Kritcher, C. V. Young, H. F. Robey, C. R. Weber, A. B. Zylstra, O. A. Hurricane, D. A. Callahan, J. E. Ralph, J. S. Ross, K. L. Baker *et al.*, "Design of inertial fusion implosions reaching the burning plasma regime," Nat. Phys. **18**, 251–258 (2022).

[25]A. B. Zylstra, O. A. Hurricane, D. A. Callahan, A. L. Kritcher, J. E. Ralph, H. F. Robey, J. S. Ross, C. V. Young, K. L. Baker, D. T. Casey *et al.*, "Burning plasma achieved in inertial fusion," Nature **601**, 542–548 (2022).

[26]R. Betti, "A milestone in fusion research is reached," Nat. Rev. Phys. **5**, 6–8 (2023).

[27]D. S. Montgomery, J. A. Cobble, J. C. Fernandez, R. J. Focia, R. P. Johnson, N. Renard-LeGalloudec, H. A. Rose, and D. A. Russell, "Recent Trident single hot spot experiments: Evidence for kinetic effects, and observation of Langmuir decay instability cascade," Phys. Plasmas **9**, 2311 (2002).

[28]J. C. Fernandez, J. A. Cobble, D. S. Montgomery, M. D. Wilke, and B. B. Afeyan, "Observed insensitivity of stimulated Raman scattering on electron density," Phys. Plasmas **7**, 3743 (2000).

[29]H. X. Vu, D. F. DuBois, and B. Bezzerides, "Transient enhancement and detuning of laser-driven parametric instabilities by particle trapping," Phys. Rev. Lett. **86**, 4306 (2001).

[30]H. X. Vu, D. F. DuBois, and B. Bezzerides, "Kinetic inflation of stimulated Raman backscatter in regimes of high linear Landau damping," Phys. Plasmas **9**, 1745 (2002).

[31]H. X. Vu, D. F. DuBois, and B. Bezzerides, "Inflation threshold: A nonlinear trapping-induced threshold for the rapid onset of stimulated Raman scattering from a single laser speckle," Phys. Plasmas **14**, 012702 (2007).

[32]B. La Fontaine, D. M. Villeneuve, H. A. Baldis, R. P. Drake, and K. Estabrook, "Test of the Landau cutoff of stimulated Raman scattering spectra as an electron-temperature diagnostic in laser-produced plasmas," Phys. Rev. Lett. **68**, 484 (1992).

[33]D. T. Michel, S. Depierreux, C. Stenz, V. Tassin, and C. Labaune, "Exploring the Saturation Levels of Stimulated Raman Scattering in the Absolute Regime," Phys. Rev. Lett. **104**, 255001 (2010).

[34]S. Depierreux, V. Yahia, C. Goyon, G. Loisel, P.-E. Masson-Laborde, N. Borisenko, A. Orekhov, O. Rosmej, T. Rienecker, and C. Labaune, "Laser light triggers increased Raman amplification in the regime of nonlinear Landau damping," Nat. Commun. **5**, 4158 (2014).

[35]Y. X. Wang, Q. Wang, C. Y. Zheng, Z. J. Liu, C. S. Liu, and X. T. He, "Nonlinear transition from convective to absolute Raman instability with trapped electrons and inflationary growth of reflectivity," Phys. Plasmas **25**, 100702 (2018).

[36]S. J. Spencer, A. G. Seaton, T. Goffrey, and T. D. Arber, "Inflationary stimulated Raman scattering in shock-ignition plasmas," Phys. Plasmas **27**, 122705 (2020).
[37]N. Rostoker and M. N. Rosenbluth, "Test particles in a completely ionized plasma," Phys. Fluids **3**(1), 1 (1960).
[38]G. Bekefi, *Radiation Processes in Plasmas* (Wiley, New York, 1966), Chap. 4.
[39]A. G. Sitenko, *Electromagnetic Fluctuations in a Plasma*, translated from Russian by M. D. Friedman (Academic Press, San Diego, 1967).
[40]N. A. Krall and A. W. Trivelpiece, *Principles of Plasma Physics* (McGraw-Hill, Inc., New York, 1973), Chap. 11.
[41]K. Papadopoulos and H. P. Freund, "Collective radio emissions from plasmas," Space Sci. Rev. **24**, 511–566 (1979).
[42]R. Schlickeiser, M. M. Martinović, and P. H. Yoon, "Subluminal electrostatic noise in isotropic space plasmas. General formulas and nonrelativistic thermal limit," Phys. Plasmas **28**, 052110 (2021).
[43]P. M. Stone and P. L. Auer, "Excitation of electrostatic waves near electron cyclotron harmonic frequencies," Phys. Rev. **138**(3A), A695–A700 (1965).
[44]R. Schlickeiser and P. H. Yoon, "Quasilinear theory of general electromagnetic fluctuations including discrete particle effects for magnetized plasmas: General analysis," Phys. Plasmas **29**(9), 092105 (2022).
[45]M. N. Rosenbluth and C. S. Liu, "Cross-field energy transport by plasma waves," Phys. Fluids **19**(6), 815 (1976).
[46]C. K. Birdsall and A. B. Langdon, *Plasma Physics via Computer Simulation* (IoP Publishing, Bristol, 2000).
[47]A. B. Langdon, "Kinetic theory for fluctuations and noise in computer simulation of plasma," Phys. Fluids **22**, 163–171 (1979).
[48]M. E. Dieckmann, A. Ynnerman, S. C. Chapman, G. Rowlands, and N. Andersson, "Simulating thermal noise," Phys. Scr. **69**, 456 (2004).
[49]T. D. Arber and R. G. Vann, "A critical comparison of Eulerian-grid-based Vlasov wolvers," J. Comput. Phys. **180**(1), 339–357 (2002).
[50]F. Filbet and E. Sonnendrücker, "Comparison of Eulerian Vlasov solvers," Comput. Phys. Commun. **150**(3), 247–266 (2003).
[51]P. Bertrand, A. Ghizzo, S. J. Karttunen, T. J. H. Pättikangas, R. R. E. Salomaa, and M. Shoucri, "Two-stage electron acceleration by simultaneous stimulated Raman backward and forward scattering," Phys. Plasmas **2**(8), 3115–3129 (1995).
[52]A. Grassi, L. Fedeli, A. Sgattoni, and A. Macchi, "Vlasov simulation of laser-driven shock acceleration and ion turbulence," Plasma Phys. Controlled Fusion **58**(3), 034021 (2016).
[53]D. L. Newman, M. V. Goldman, R. E. Ergun, L. Andersson, and N. Sen, "Reduced Vlasov simulations in higher dimensions," Comput. Phys. Commun. **164**, 122 (2004).
[54]H. A. Rose and W. Daughton, "Vlasov simulation in multiple spatial dimensions," Phys. Plasmas **18**, 122109 (2011).
[55]B. Eliasson, C. S. Liu, X. Shao, R. Z. Sagdeev, and P. K. Shukla, "Laser acceleration of monoenergetic protons via a double layer emerging from an ultra-thin foil," New J. Phys. **11**, 073006 (2009).
[56]T. D. Arber, K. Bennet, C. S. Brady, A. Lawrence-Douglas, M. G. Ramsay, N. J. Sircombe, P. Gillies, R. G. Evans, H. Schmitz, A. R. Bell, and C. P. Ridgers, "Contemporary particle-in-cell approach to laser-plasma modelling," Plasma Phys. Controlled Fusion **57**, 113001 (2015).
[57]K. Bennett (2021). "User manual for the EPOCH PIC codes," Github. https://github.com/Warwick-Plasma/EPOCH_manuals/releases
[58]C. Z. Cheng and G. Knorr, "The integration of the Vlasov equation in configuration space," J. Comput. Phys. **22**, 330–351 (1976).
[59]G. Manfredi, "Long-time behavior of nonlinear Landau damping," Phys. Rev. Lett. **79**, 2815–2818 (1997).
[60]B. Eliasson, "Numerical simulations of the Fourier-transformed Vlasov–Maxwell system in higher dimensions—theory and applications," Transp. Theor. Stat. Phys. **39**(5), 387–465 (2010).
[61]W. L. Kruer, "Laser plasma interactions with intensities from $10^{12} - 10^{21}$ W/cm^2," Phys. Plasmas **10**(5), 2087–2092 (2003).
[62]R. J. Goldston and P. H. Rutherford, *Introduction to Plasma Physics* (IoP, Bristol 1995).
[63]M. N. Rosenbluth, R. B. White, and C. S. Liu, "temporal evolution of a three-wave parametric instability," Phys. Rev. Lett. **31**, 1190 (1973).
[64]T. H. Stix, *Waves in Plasmas* (AIP, New York, 1992), Chap. 9.
[65]H. Liang, Z. J. Liu, C. Y. Zheng, X. Jiang, F. Wu, X. Y. Hu, and B. Li, "Study of stimulated Raman and Brillouin scattering in a finite interaction region under the convective instability condition," Chin. Sci. Bull. **57**, 2747–2751 (2012).
[66]B. D. Fried and S. D. Conte, *The Plasma Dispersion Function* (Academic Press, New York, 1961).
[67]H. G. Dawson, "On the numerical value of $\int_0^\infty e^{x^2} dx$," Proc. London Math. Soc. **s1-29**, 519–522 (1897).
[68]J. H. McCabe, "A continued fraction expansion with a truncation error estimate for Dawson's integral," Math. Comput. **28**, 811–816 (1974).
[69]S. Sýkora, Dawson integral approximations, Stan's Library, 2012.
[70]J. Dawson and C. Oberman, "High-frequency conductivity and the emission and absorption coefficients of a fully ionized plasma," Phys. Fluids **5**, 517–524 (1962).
[71]R. Z. Sagdeev and A. A. Galeev, *Nonlinear Plasma Theory*, edited by T. M. O'Neil and D. L. Book (Benjamin, New York, 1969).
[72]F. Valentini, D. Perrone, F. Califano, F. Pegoraro, P. Veltri, P. J. Morrison, and T. M. O'Neil, "Undamped electrostatic plasma waves," Phys. Plasmas **19**, 092103 (2012).
[73]W. L. Kruer, J. M. Dawson, and R. N. Sudan, "Trapped-particle instability," Phys. Rev. Lett. **23**, 838 (1969).
[74]M. Brunetti, F. Califano, and F. Pegoraro, "Asymptotic evolution of nonlinear Landau damping," Phys. Rev. E **62**, 4109 (2000).
[75]M. E. Dieckmann, P. Ljung, A. Ynnerman, and K. G. McClements, "Large-scale numerical simulations of ion beam instabilities in unmagnetized astrophysical plasmas," Phys. Plasmas **7**, 5171 (2000).
[76]M. N. Rosenbluth and C. S. Liu, "Excitation of plasma waves by two laser beams," Phys. Rev. Lett. **29**, 701 (1972).
[77]C. J. McKinstrie, R. E. Giacone, and E. A. Startsev, "Accurate formulas for the Landau damping rates of electrostatic waves," Phys. Plasmas **6**(2), 463–466 (1999).